



22 can result in reduced surface area to either the solid-state electrolyte or the electron-conducting  
23 phase, resulting in increased charge transfer and ohmic resistance, respectively [17–19].

24 Because a significant amount of cathode capacity-fade mechanisms are related to secondary-  
25 particle cracking, researchers typically evaluate cathode “aging” through qualitative crack anal-  
26 ysis [12, 28]. Cathode particle cracking can occur for different reasons. First, during manu-  
27 facturing, cathode cracking can occur during the calendaring process [7, 31, 32]. The cracks  
28 formed during calendaring typically originate at particle/particle or particle/current-collector  
29 contacts and tend to form long cracks that cleave particles. Second, cathode cracking can oc-  
30 cur during formation cycles due to non-ideal primary particle grain orientations. These initial  
31 “break-in” cracks tend to be small and are significantly influenced by the grain shapes, sizes, and  
32 orientations [33, 34]. Break-in cracking is currently the primary focus for physics-based chemo-  
33 mechanical models [33, 35–38]. Finally, cracks can form during operation when the cathodes are  
34 cycled at higher voltage ranges, either due to increased voltage bounds or due to voltage slip-  
35 page [12, 39]. At high voltages or during high delithiation demands, the lithium concentration  
36 on the cathode surface can drop below a minimum concentration threshold causing irreversible  
37 reconstruction of the host crystal. This reconstruction reduces the specific capacity and induces  
38 significant local stain, leading to secondary-particle cracking [29, 33].

39 Currently, structural post-mortem analysis of cathode particle fracture is primarily conducted  
40 using 2D scanning electron microscope (SEM) images and X-ray techniques [11, 12, 29, 40–42].  
41 Since a quantitative analysis of such 2D images can be difficult, the comparison of differently  
42 aged post-mortem cathodes is often performed by means of visual inspection [11, 12, 30]. Such a  
43 qualitative analysis is typically accompanied by quantitative electrochemical analysis (e.g., elec-  
44 trochemical impedance spectroscopy, incremental capacity analysis [12, 29]) and post-mortem,  
45 atomistic-scale surface-sensitive techniques [11, 20, 29, 42, 43]. However, relying on qualita-  
46 tive cracking-extent assessments introduces subjectivity in the analysis, highlighting the need  
47 for more quantitative and reproducible methods to characterize cathode-particle fracture. A  
48 quantitative analysis of cracks in 2D SEM data has been conducted, e.g., in [40, 41]. However,  
49 2D images of cracked particles depict only planar sections of the actual 3D microstructure. In  
50 other words, a 2D slice of a cathode electrode represents just a small portion of the 3D system,  
51 which includes out-of-plane features such as tortuous crack connections.

52 In contrast to 2D crack analysis, it is significantly more difficult to segment and identify crack  
53 structures in 3D images [44, 45] and to reassemble fragments of fractured particles [46]. This  
54 increased difficulty is due to the fact that 3D imaging (e.g., via nano-CT) is often accompanied  
55 with a lower resolution than 2D microscopy techniques (e.g., SEM), which produce image data  
56 on a similar length scale—i.e., fine structures caused by cracks often exhibit a bad contrast in 3D  
57 image data. Moreover, a quantitative crack analysis requires computation of metrics to describe  
58 cracks in 3D [47]. Unfortunately, the necessary 3D imaging equipment is expensive and often  
59 less available than comparable 2D imaging equipments and their analysis tools [20, 48, 49]. A  
60 potential remedy is provided by stochastic 3D modeling, which can generate countless virtual  
61 NMC particles exhibiting statistically similar properties as the relatively low number of particles  
62 that have been imaged in 3D [50]. In general, realizations of stochastic 3D models for material  
63 microstructures, such as those proposed in [51, 52], can serve as geometry inputs for mechanical  
64 and electrochemical simulations. These simulations can help to investigate properties like crack  
65 propagation in materials and their elastostatic or -plastic responses [33, 53–55]. By performing  
66 such simulation studies on generated morphologies quantitative structure-property relationships  
67 can be derived [56, 57].

68 As mentioned above, measured 3D image data is not always accessible. Therefore approaches  
69 have been developed to calibrate stochastic 3D models utilizing only 2D image data [58]. Re-  
70 cently, a stochastic nanostructure model based on generative adversarial networks (GAN) was  
71 introduced, which mimics the 3D polycrystalline grain architecture of non-cracked NMC parti-  
72 cles [59] by only using 2D electron backscatter diffraction (EBSD) cross sections for calibration.  
73 In the present paper, a stochastic 3D model is proposed that can generate realistic cracks in  
74 virtual polycrystalline NMC particles, which propagate along grain boundaries. Similar to the  
75 approach considered in [60], our model is based on random tessellations, where certain facets are  
76 dilated to mimic cracks. In this work, a facet between two grains is either intact or fully cracked  
77 without intermediate case (that is all surface elements of the facet are either intact or cracked).  
78 The model is calibrated and validated by comparing planar cross sections of the stochastic 3D  
79 crack network model with 2D SEM image data, utilizing several geometric descriptors charac-  
80 terizing the morphology of the crack phases. Additionally, to emphasize the strength of our  
81 stereological modeling approach, geometric descriptors related to effective battery properties  
82 are determined, which cannot be reliably derived from 2D images.

## 83 2. MATERIALS AND IMAGE PROCESSING

84 The focus of this section is to describe the materials considered in the present paper, as  
85 well as on the processing of 2D SEM image data of these materials. First, in Section 2.1,  
86 the cathode materials and their cycling history are discussed. Then, in Section 2.2, several  
87 image processing techniques are described, where gray-scale images of planar cross sections  
88 of the cathodes, obtained by SEM imaging, are phasewise segmented using a 2D U-net and,  
89 afterwards, particlewise segmented utilizing a marker-based watershed transform. Additionally,  
90 morphological operations are used to denoise the crack phase. Finally, in Section 2.3, the set of  
91 segmented 2D images is decomposed into two subsets, based on the predominance of short or  
92 long cracks. Later on, in Section 4 the introduced crack model is calibrated to both subsets, to  
93 reproduce the wide structural variability of cracked NMC particles.

94 **2.1. Electrode materials and cycling history.** The active electrode material used in the  
95 present paper consisted of  $\text{LiNi}_{0.5}\text{Mn}_{0.3}\text{Co}_{0.2}\text{O}_2$  (NMC532) and was taken from the same batch  
96 of cells cycled in our previous work [41], where the particles had similar polycrystalline archi-  
97 tectures as those shown in [61]. The electrodes consisted of 90 wt% NMC532, 5wt% Timcal  
98 C45 carbon and 5wt% Solvay 5130 PVDF binder. The coating thickness was 62  $\mu\text{m}$  with 26.1%  
99 porosity.

100 The cell was formed by charging to 1.5 V, holding at open-circuit for 12 hours, and then  
101 cycling 3 times between 3 V and 4.1 V using a protocol consisting of C/2 constant-current and  
102 constant-voltage at 4.1 V until the current dropped below C/10. The cells were then degassed,  
103 resealed, and prepared for fast charging at 20 °C. Subsequently, the cells were cycled using a  
104 protocol of fast charging at 6C constant current between 3 V and 4.1 V followed by constant-  
105 voltage hold until 10 minutes total charge time had elapsed. Charge was followed by 15 minutes  
106 of open circuit and discharge at C/2 to 3 V, followed by a final rest for 15 minutes. The materials  
107 used in this paper were cycled 200 times under these conditions.

108 **2.2. Preprocessing and analysis of 2D SEM image data.** The NMC electrode material  
109 was removed from the cells and a small sample cut from the electrode sheet. The sample was

110 then cross sectioned using an Ar-ion beam cross-sectional polisher (JOEL CP19520). The cross-  
 111 sectioned face was then imaged in an SEM system with a pixel size of 38.5 nm. A representative  
 112 cross section, derived by SEM imaging, is presented in Figure 1 (top).

113 For image processing, we first describe the image processing steps which were performed  
 114 in [41] to segment the 2D SEM image data of the cross sections with respect to phases and  
 115 particles, i.e., each pixel is classified either as solid phase, crack phase or background, where  
 116 each particle is assigned with a unique label. Note that the raw image data depicted scale bars  
 117 for indicating the corresponding length scales (which have been produced by the microscope’s  
 118 software). Since the scale bars can adversely impact subsequent image processing steps, the  
 119 *inpainting\_biharmonic* method of the scikit-image package in Python [62] has been utilized to  
 120 remove scale bars. Then, a generative adversarial network [63] has been deployed to increase the  
 121 resolution (super-resolution) such that pixel sizes of 14.29 nm have been achieved, facilitating  
 122 the assignment of pixels to phases (i.e., solid phase, crack phase, background).

123 To obtain a phasewise segmentation, a 2D U-net was deployed to classify the phase affiliation  
 124 for each pixel in 2D SEM cross sections. More precisely, the network’s output is given by  
 125 pixelwise probabilities of phase membership. By deploying thresholding techniques onto these  
 126 pixelwise probabilities, a phase-wise segmentation has been obtained, see [41] for further details.  
 127 In particular, Figure 1 indicates that the data has been segmented reasonably well, i.e., only  
 128 a low, statistically negligible number of particles (see bottom left) exhibits larger misclassified  
 129 areas.

130 The particle-wise segmentation was obtained by means of a marker-based watershed trans-  
 131 form on the Euclidean distance transform, denoted by  $D$  in the following. More precisely,  
 132  $D: W \rightarrow \mathbb{R}_+ = [0, \infty)$  is a mapping, which assigns each pixel  $x \in W$  its distance to the back-  
 133 ground phase. Here,  $W \subset \mathbb{Z}_\rho^2$  represents the sampling window, where  $\mathbb{Z}_\rho = \{\dots, -\rho, 0, \rho, \dots\}$   
 134 and  $\rho > 0$  denotes the pixel length. Note that the watershed function of the Python package  
 135 scikit-image [62] was deployed on  $-D$ , where the markers (i.e., the positions of particles to  
 136 be segmented) are obtained by thresholding  $D$  at some distance level  $r > 0$ , where  $r$  is set  
 137 equal to 50 pixels. After the application of the watershed algorithm, truncated particles were  
 138 removed in order to avoid edge effects. In addition, we removed regions within the segmented  
 139 image that may have resulted from oversegmentation or falsely segmented phases, which can  
 140 occur due to shine-through effects during SEM imaging. To identify such regions, we first used  
 141 the *GaussianMixture* method from the scikit-learn package in Python [64]. This method was  
 142 employed to fit a mixed bivariate Gaussian distribution (with two components) to the pairs of  
 143 area-equivalent diameters and eccentricity values of the segmented regions in the image [62].  
 144 Note that the eccentricity of a segmented region is defined as the eccentricity of a fitted ellipse  
 145 that has the same first and second moments. After fitting the mixed Gaussian distribution,  
 146 its first component, i.e., a bivariate Gaussian distribution, exhibited a mean value vector com-  
 147 prising a relatively large area-equivalent diameter and low eccentricity (which corresponds to  
 148 circular regions). We assumed that this component corresponds to correctly segmented par-  
 149 ticles in the image. In contrast, the second component, characterized by a mean vector with  
 150 smaller area-equivalent diameters and higher eccentricity, was assumed to represent incorrect  
 151 segmentations. Consequently, we removed regions from the segmentations for which the vector  
 152 of area-equivalent diameter and eccentricity was more likely to belong to the second component,  
 153 as determined by the fitted Gaussian mixture model.

154 Note that a few particles affected by shine-through effects from SEM imaging remain. However,  
 155 their small proportion has a negligible impact on the overall statistical properties of the particle

156 set. This procedure is performed on 13 SEM cross sections, each consisting of  $5973 \times 3079$  pixels,  
 157 which corresponds to approximately  $85 \mu\text{m} \times 44 \mu\text{m}$  with a resolution of  $\rho = 14.29 \text{ nm}$ . Note that  
 158 these 13 cross sections are derived from the same cathode and are partly overlapping. In each  
 159 cross section, between 43 and 60 particles were detected. An exemplary phasewise segmented  
 160 cross section is shown in Figure 1 (bottom).

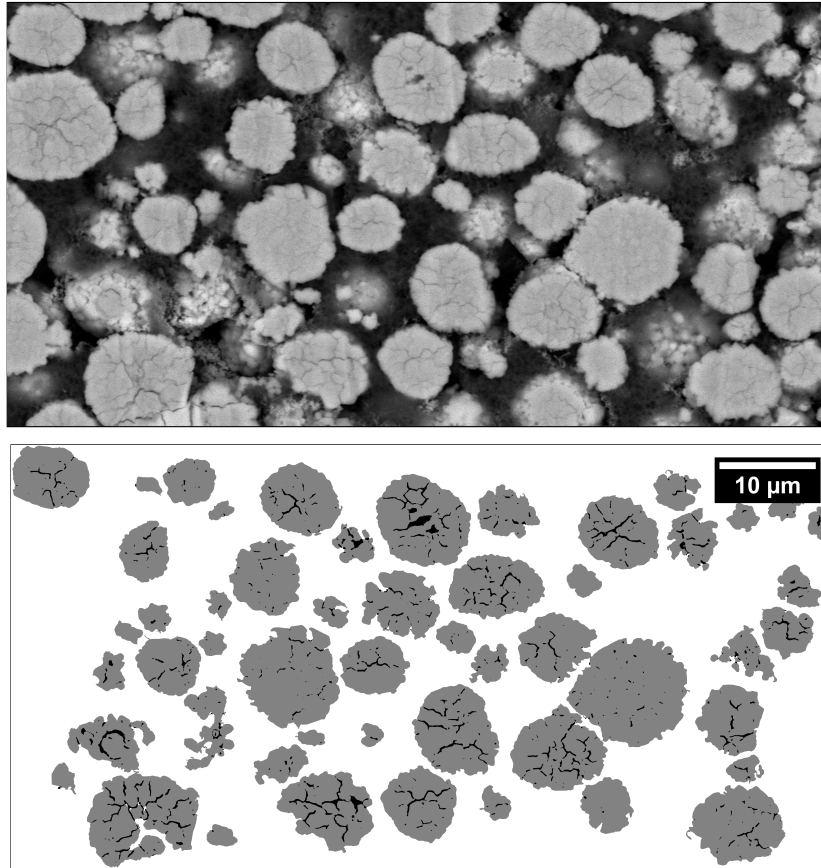


FIGURE 1. 2D SEM image (top) and its phasewise segmentation (bottom), where each pixel is classified as background (white), solid (gray) or crack (black). Note that truncated and small particles with a large eccentricity have been removed.

161 In addition to the preprocessing procedure explained above and proposed in [41], the following  
 162 data processing steps have been carried out. First, since some SEM images depict overlapping  
 163 areas, duplicates were removed. More precisely, all pairs of particles from overlapping images  
 164 were registered, i.e., for each pair of particles a rigid transformation is determined which max-  
 165 imizes the correspondence of the first particle after application of the transformation with the  
 166 second particle, where the agreement is measured by means of the cross correlation in scikit-  
 167 image [62]. If pairs of registered particles exhibit a large correspondence, a duplicate is detected,  
 168 which is omitted in further analysis. Furthermore, to reduce the number of very small cracks,  
 169 e.g., caused by noise or by several connected components of the crack phase that actually belong  
 170 to the same crack, morphological opening, followed by morphological closing, was performed  
 171 on the crack phase. For both morphological operations, a disk-shaped structuring element with  
 172 radius  $r_o = 1$  for opening and  $r_c = 3$  for closing was used.

173 In summary, the image processing procedure described above resulted into 506 images depicting  
 174 ing the phasewise segmentation of NMC particles in planar sections, i.e., each pixel is classified  
 175 either as solid (active NMC material), crack, or background. Each of these images depicts a  
 176 single cross section of a NMC particle, which shows a certain network of cracks. In the following  
 177 sections, an individual particle is denoted by  $P_{\text{ex}}$ .

178 **2.3. Decomposition of the set of segmented particles into two subsets.** In this section  
 179 we explain how the set of segmented particles, described in Section 2.2, is decomposed into two  
 180 subsets with predominantly long and short cracks, respectively. This subdivision is motivated by  
 181 the structural heterogeneity observed in the crack networks of segmented particle cross sections.  
 182 In Section 4, the stochastic crack model that is introduced in Section 3, is fitted separately to  
 183 both subsets.

184 For this classification, for each particle  $P_{\text{ex}}$ , we consider a continuous representation in the  
 185 two-dimensional Euclidean space  $\mathbb{R}^2$ , denoting its solid phase by  $\Xi_{\text{solid}}^{(\text{ex})} \subset \mathbb{R}^2$  and its crack phase  
 186 by  $\Xi_{\text{crack}}^{(\text{ex})} \subset \mathbb{R}^2$ , where each pixel of  $P_{\text{ex}}$  is considered as patch (i.e., as a square subset of  $\mathbb{R}^2$ ).  
 187 Thus, in the following we will write

$$P_{\text{ex}} = (\Xi_{\text{solid}}^{(\text{ex})}, \Xi_{\text{crack}}^{(\text{ex})}) \quad (1)$$

188 for the continuous representation of a particle. Furthermore, by  $\mathcal{G}$  we denote the set of continu-  
 189 ous representations of all 506 particles. The dataset  $\mathcal{G}$  is comprised of particles with sizes ranging  
 190 from 1.39  $\mu\text{m}$  to 13.62  $\mu\text{m}$  (in terms of their area-equivalent diameters, denoted by  $\text{aed}(P_{\text{ex}})$ ).

191 By visual inspection of segmented particles, it becomes apparent that the crack networks  
 192 of some particles consist predominantly of short and others of long cracks, see Figures 1 and 2.  
 193 Motivated by these morphological differences, the set  $\mathcal{G}$  is subdivided into two disjoint subsets,  
 194  $\mathcal{G}_{\text{short}}$  and  $\mathcal{G}_{\text{long}}$ . To decide for a given particle  $P_{\text{ex}}$  if it belongs to  $\mathcal{G}_{\text{short}}$  or  $\mathcal{G}_{\text{long}}$ , a skeletonization  
 195 algorithm [65] was applied to the crack phase of  $P_{\text{ex}}$ , where each connected component of the  
 196 crack phase  $\Xi_{\text{crack}}$  is represented by its center line, which we refer to as a skeleton segment. The  
 197 family of all skeleton segments of a particle  $P_{\text{ex}}$  is called skeleton and denoted by  $\mathcal{S}(P_{\text{ex}})$ .

198 If the longest crack skeleton segment of a particle  $P_{\text{ex}}$  is shorter than or equal to  $t \cdot \text{aed}(P_{\text{ex}})$   
 199 for some threshold  $t > 0$ , then  $P_{\text{ex}}$  is assigned to  $\mathcal{G}_{\text{short}}$ , otherwise  $P_{\text{ex}}$  is assigned to  $\mathcal{G}_{\text{long}}$ . Note  
 200 that the area-equivalent diameter  $\text{aed}(P)$  of particle  $P_{\text{ex}}$  is given by

$$\text{aed}(P_{\text{ex}}) = \sqrt{\frac{4 \nu_2(\Xi_{\text{solid}} \cup \Xi_{\text{crack}})}{\pi}},$$

201 where  $\nu_2(A)$  denotes the 2-dimensional Lebesgue measure, i.e., the area of a set  $A \subset \mathbb{R}^2$ . Thus,  
 202 formally, the sets  $\mathcal{G}_{\text{short}}$  and  $\mathcal{G}_{\text{long}}$  can be written as

$$\mathcal{G}_{\text{short}} = \{P_{\text{ex}} \in \mathcal{G} : \max_{S \in \mathcal{S}(P_{\text{ex}})} \mathcal{H}_1(S) \leq t \cdot \text{aed}(P_{\text{ex}})\} \quad \text{and} \quad \mathcal{G}_{\text{long}} = \mathcal{G} \setminus \mathcal{G}_{\text{short}}$$

203 where  $\mathcal{H}_1(S)$  denotes the 1-dimensional Hausdorff measure of a skeleton segment  $S \in \mathcal{S}(P_{\text{ex}})$ ,  
 204 which corresponds to the length of  $S$ <sup>1</sup>. It turned out that  $t = 0.55$  is a reasonable choice,  
 205 which splits  $\mathcal{G}$  into two subsets  $\mathcal{G}_{\text{short}}$  and  $\mathcal{G}_{\text{long}}$ , each containing particles from the entire range  
 206 of observed particle sizes, where  $\mathcal{G}_{\text{short}}$  comprises 423 particles and  $\mathcal{G}_{\text{long}}$  consists of 83 particles.  
 207 For larger values of  $t$  the statistical representativeness of  $\mathcal{G}_{\text{long}}$  diminishes, whereas for smaller  
 208 values of  $t$  we observed that the resulting set  $\mathcal{G}_{\text{long}}$  was comprised of particles with relatively small  
 209 cracks—which would have made the decomposition of particles into  $\mathcal{G}_{\text{short}}$  and  $\mathcal{G}_{\text{long}}$  redundant.

<sup>1</sup>The length of a skeleton segment was approximated by the number of pixels multiplied with the resolution of  $\rho = 14.29 \text{ nm}$ .

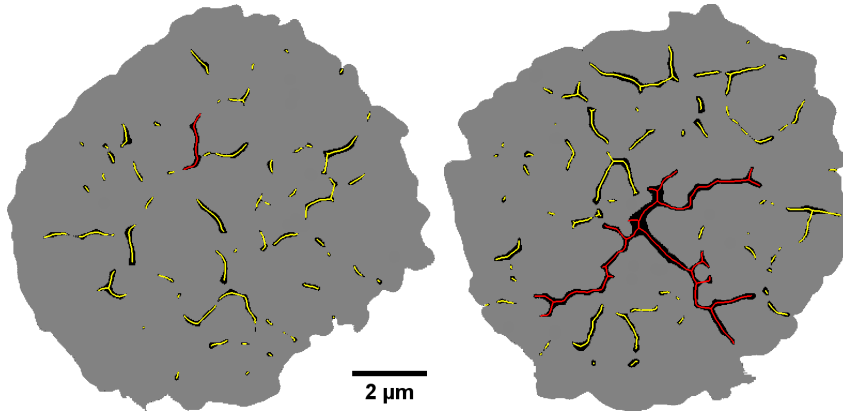


FIGURE 2. Segmented NMC particles together with their skeletons (yellow), where the skeleton segment of the longest crack is highlighted in red. The particle on the left-hand side belongs to  $\mathcal{G}_{\text{short}}$ , consisting of predominantly short cracks, while the particle on the right-hand side belongs to  $\mathcal{G}_{\text{long}}$ , exhibiting long cracks.

210

### 3. STOCHASTIC 3D MODEL FOR CRACKED NMC PARTICLES

211 In this paper, a stochastic 3D model is proposed, which generates cracks in (simulated) pris-  
 212 tine MNC particles hierarchically on different length scales. Two different kinds of data are used  
 213 as model inputs. First, to generate pristine NMC particles in 3D, exhibiting a polycrystalline  
 214 inner structure, we draw samples from the stochastic particle model introduced in [50]. Then,  
 215 we use 2D SEM image data to stereologically calibrate a stochastic 3D model for adding cracks,  
 216 where we assume that cracks propagate along the polycrystalline grain boundaries through the  
 217 particles without having a preferred direction. It is important to emphasize that the proposed  
 218 stochastic crack model generates virtual, but realistic cracked NMC particles in 3D, even though  
 219 it is calibrated using only 2D image data.

220 In Section 3.1, the main features of the stochastic 3D model proposed in [50] are summa-  
 221 rized, which is used to generate the virtual, pristine NMC particles. To efficiently represent  
 222 the neighborhood relationships of individual grains of a particle, in Section 3.2 a graph-based  
 223 data structure is introduced by means of Laguerre tessellations. Subsequently, in Section 3.3, a  
 224 stochastic model is presented, which incorporates single cracks into the (previously simulated)  
 225 pristine NMC particles, utilizing the graph-based representation via tessellations stated in Sec-  
 226 tion 3.2. Then, in Section 3.4, it is shown how the single-crack model can be applied multiple  
 227 times to generate a random crack network consisting of several cracks within a given parti-  
 228 cle. Finally, in Section 3.5, an extended stochastic crack network model is presented, which is  
 229 deployed for modeling the entire crack phase of NMC particles in 3D.

230 **3.1. Stochastic 3D model for pristine polycrystalline NMC particles.** In [50] a spatial  
 231 stochastic model for the 3D morphology of pristine polycrystalline NMC particles has been  
 232 developed and calibrated by means of tomographic image data. More precisely, nano-CT data  
 233 depicting the outer shell of NMC particles has been leveraged to calibrate a random field model  
 234 on the three-dimensional sphere, whose realizations are virtual outer shells of NMC particles  
 235 that are statistically similar to those observed in the nano-CT data. Furthermore, a random  
 236 Laguerre tessellation model for the inner grain architecture of NMC particles (which lives on a  
 237 smaller length scale) has been calibrated using 3D EBSD data.

238 Note that a Laguerre tessellation in  $\mathbb{R}^3$  is a subdivision of the three-dimensional Euclidean  
 239 space (or some sampling window within  $\mathbb{R}^3$ ) that is given by some marked point pattern  
 240  $\{(s_n, r_n), n \in \mathbb{N}\}$ , where  $s_n \in \mathbb{R}^3$  is called a seed or generator point, and  $r_n \in \mathbb{R}$  is an (ad-  
 241 ditive) weight, for each  $n \in \mathbb{N} = \{1, 2, \dots\}$ , see [66, 67]. The interior of the grain generated by  
 242 the  $n$ -th marked seed point  $(s_n, r_n)$  of a Laguerre tessellation is defined as set of points  $x \in \mathbb{R}^3$ ,  
 243 which are closer to  $s_n$  than to all other seed points  $s_k$ ,  $k \neq n$ , with respect to the “distance  
 244 function”  $d: \mathbb{R}^3 \times \mathbb{R}^4 \rightarrow \mathbb{R}$  given by  $d(x, (s, r)) = |x - s| - r$  for all  $x, s \in \mathbb{R}^3$  and  $r \in \mathbb{R}$ , where  
 245  $|\cdot|$  denotes the Euclidean norm in  $\mathbb{R}^3$ .<sup>2</sup> Thus, formally, the grain  $g_n \subset \mathbb{R}^3$  generated by the  
 246  $n$ -th marked seed point  $(s_n, r_n)$  is given by

$$g_n = \left\{ x \in \mathbb{R}^3 : d(x, (s_n, r_n)) \leq d(x, (s_k, r_k)) \quad \text{for all } k \neq n \right\}. \quad (2)$$

247 To compute grains  $g_n$  for a given set of marked seed points we use the GeoStoch library [68].

248 Both stochastic models mentioned above, i.e., the random field model for the outer shell and  
 249 the random tessellation model for the inner grain architecture, have been combined in [50],  
 250 to derive a multi-scale 3D model for pristine NMC particles with full inner grain architecture.  
 251 Thus, in the first modeling step of the present paper, we will draw realizations from the multi-  
 252 scale 3D model of [50] for the generation of virtual pristine NMC particles, to which cracks will  
 253 be added in the subsequent modeling steps. Using an analogous notation like that considered  
 254 in Eq. (1), the simulated pristine NMC particles will be denoted by  $P_{\text{pr}} = (\Xi_{\text{solid}}^{(\text{pr})}, \emptyset)$ , where

$$\Xi_{\text{solid}}^{(\text{pr})} = \bigcup_{n \in I} g_n \subset \mathbb{R}^3$$

255 for some index set  $I \subset \mathbb{N}$ . The stochastic crack model introduced later on (in Sections 3.3 to 3.5)  
 256 assigns facets, i.e. planar grain boundary segments, of the pristine particle  $P_{\text{pr}}$  with crack widths  
 257 to introduce a crack network. To do so, we first derive an alternative graph representation of  
 258 the Laguerre tessellation  $\{g_n, n \in I\}$  which describes the grain architecture of  $P_{\text{pr}}$ .

259 **3.2. Graph representation of pristine grain architectures.** In the literature, a Laguerre  
 260 tessellation in  $\mathbb{R}^3$  is usually given by a collection of grains  $g_n \subset \mathbb{R}^3$  as defined in Eq. (2).  
 261 However, alternatively, such a tessellation can be represented as a collection of planar facets  
 262 given by

$$g_n \cap g_k = \{x \in \mathbb{R}^3 : d(x, (s_n, r_n)) = d(x, (s_k, r_k))\}$$

263 for  $n, k \in \mathbb{N}$  with  $n \neq k$  and  $\mathcal{H}_2(g_n \cap g_k) > 0$ , where  $\mathcal{H}_2(g_n \cap g_k)$  is the 2-dimensional Hausdorff  
 264 measure of  $g_n \cap g_k \subset \mathbb{R}^3$ , which corresponds to the area of  $g_n \cap g_k$ . Thus, the sets  $g_n \cap g_k$  are  
 265 convex plane segments being the intersection of neighboring grains, the union of which is equal  
 266 to the union of the boundaries  $\partial g_n$  of the convex polyhedra  $g_n$  considered in Eq. (2).

267 Furthermore, to describe the neighborhood structure of the facets, we consider the so-called  
 268 neighboring facet graph, denoted by  $G = (F, E)$ . The set  $F$  of its vertices is the collection of  
 269 planar facets of the Laguerre tessellation, and  $E$  is its set of edges, where two facets  $f, f' \in F$   
 270 are connected by an edge  $e \in E$  if they are adjacent, which means that  $f \cap f'$  is a line segment  
 271 with positive length, i.e.,  $\mathcal{H}_1(f \cap f') > 0$ , see Figures 3a and 3b.

272 **3.3. Single crack model.** In this section, we describe the stochastic model which will be  
 273 used for the insertion of single cracks into virtual NMC particles, whose polycrystalline grain  
 274 architecture is given by a Laguerre tessellation within a certain (bounded) sampling window

<sup>2</sup>In the mathematical literature, the grains of a Laguerre tessellation are often called “cells”. However, for modeling the polycrystalline materials considered in the present paper, the wording “grain” is used.

275  $W \subset \mathbb{R}^3$ , as stated in Section 3.1, and represented by the neighboring facet graph  $G = (F, E)$   
 276 introduced in Section 3.2.

277 Assuming that cracks propagate along grain boundaries [27], we will model cracks as collec-  
 278 tions of dilated adjacent facets. With regard to the graph-based representation of tessellations  
 279 stated in Section 3.2, this means that a subset  $C \subset F$  will be chosen such that for each pair  
 280  $f, f' \in C$  with  $f \neq f'$ , there exists a sequence of adjacent facets  $f_1, \dots, f_n \in C$  such that  
 281  $f_1 = f$  and  $f_n = f'$ . This allows generating, if desired, particles with a relatively low quantity  
 282 of cracked facets, but with relatively long contiguous cracks, which would be not possible with  
 283 a stochastic approach not considering sequences of adjacent facets.

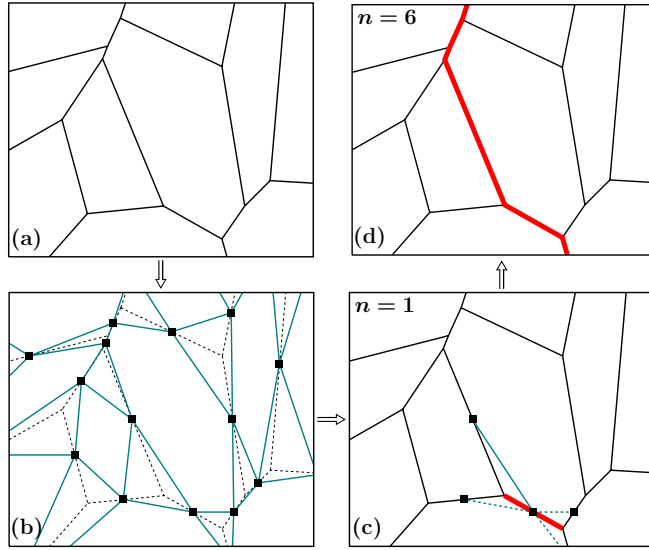


FIGURE 3. 2D scheme of the workflow to generate an individual crack along grain boundaries. For a (Laguerre) tessellation within a bounded sampling window (a), the neighboring facet graph is determined, i.e., facets are considered to be vertices of the graph (black rectangles), which are connected by edges (blue) if the underlying facets are adjacent (b). An initial facet (red) is chosen at random and assigned to the set  $C$  of crack facets (c). Iteratively, the  $n$ -th neighboring facet which is aligned “best” with the set  $C$  is assigned to it (d).

284 More precisely, to generate a set of dilated crack facets as described above, an algorithm is  
 285 proposed consisting of the following steps:

- 286 (i) Initialize the set of crack facets, putting  $C = \emptyset$ .  
 287 (ii) Generate the number  $n_{\text{facets}} \in \mathbb{N}$  of crack facets, drawing a realization  $\hat{n}_{\text{facets}} > 0$  from  
 288 a Weibull distributed random variable  $N_{\text{facets}}$  with some scale parameter  $\lambda_{\text{W}} > 0$  and  
 289 shape parameter  $k_{\text{W}} > 0$ , and putting  $n_{\text{facets}} = \text{round}(\hat{n}_{\text{facets}})$ , where

$$\text{round}(\hat{n}_{\text{facets}}) = \begin{cases} \lfloor \hat{n}_{\text{facets}} \rfloor & \text{if } \hat{n}_{\text{facets}} - \lfloor \hat{n}_{\text{facets}} \rfloor < 0.5, \\ \lfloor \hat{n}_{\text{facets}} \rfloor + 1 & \text{else,} \end{cases} \quad (3)$$

290 which means rounding to the closest integer, with  $\lfloor \hat{n}_{\text{facets}} \rfloor$  denoting the largest integer  
 291 being smaller than  $\hat{n}_{\text{facets}}$ .

- 292 (iii) Choose an initial facet  $f \in F$  at random and assign it to the set of crack facets  $C$ .  
 293 Furthermore, let  $g : F \rightarrow \mathbb{R}^3$  denote a function, which maps a facet  $f \in F$  onto its  
 294 normal vector  $v = (v_1, v_2, v_3)$  with length 1 and  $v_1 \geq 0$ .

- 295 (iv) Compute the average normal vector  $v_C = \sum_{f \in C} g(f) / |\sum_{f \in C} g(f)|^{-1}$ , to control the  
 296 alignment of the next facet, to be assigned to  $C$ .  
 297 (v) Determine the set  $A = \{f \in F \setminus C : f \cap f' \in E \text{ for some } f' \in C\} \subset F \setminus C$ , containing  
 298 the facets that are adjacent to  $C$ , but not contained in  $C$ .  
 299 (vi) Add the facet  $f \in A$  given by

$$f = \operatorname{argmax}_{f \in A} |\langle g(f), v_C \rangle| \quad (4)$$

- 300 to  $C$ , for which the normal  $g(f)$  has the best directional alignment with the average  
 301 normal vector  $v_c$  computed in step (iv), where  $\langle \cdot, \cdot \rangle$  denotes the dot product.  
 302 (vii) Repeat steps (iv) to (vi) until  $\#C = n_{\text{facets}}$ , where  $\#$  denotes cardinality.  
 303 (viii) Draw a realization  $\delta > 0$  from a gamma distributed random variable  $\Delta$  with some shape  
 304 parameter  $k_\Gamma > 0$  and scale parameter  $\theta_\Gamma > 0$ .  
 305 (ix) Dilate each crack facet  $f \in C$  using the structuring element  $B_\delta = \{x \in \mathbb{R}^3 : |x| \leq \delta/2\}$ ,  
 306 and determine the set  $\bigcup_{f \in C} (f \oplus B_\delta)$ , where  $\oplus$  denotes Minkowski addition. Note that  
 307 the set  $\bigcup_{f \in C} (f \oplus B_\delta)$  represents a crack where each facet  $f \in C$  is dilated with the same  
 308 thickness  $\delta$ .

309 This algorithm is visualized in Figure 3.

310 In summary, the stochastic model for single cracks described above is characterized by the  
 311 4-dimensional parameter vector  $\theta_1 = (\lambda_W, k_W, k_\Gamma, \theta_\Gamma) \in \mathbb{R}_+^4$ , where  $\lambda_W$  and  $k_W$  control the  
 312 length of cracks, whereas  $k_\Gamma$  and  $\theta_\Gamma$  affect their thickness.

313 Recall that in Section 3.1 we introduced the notation  $P_{\text{pr}} = (\Xi_{\text{solid}}^{(\text{pr})}, \emptyset)$  for simulated pristine  
 314 NMC particles. Analogously, for a given pristine particle  $P_{\text{pr}} = (\Xi_{\text{solid}}^{(\text{pr})}, \emptyset)$ , a particle with  
 315 a single crack will be denoted by  $P_{\theta_1} = (\Xi_{\text{solid}}^{(\theta_1)}, \Xi_{\text{crack}}^{(\theta_1)})$ , where  $\Xi_{\text{solid}}^{(\theta_1)} \cup \Xi_{\text{crack}}^{(\theta_1)} = \Xi_{\text{solid}}^{(\text{pr})}$ , with  
 316  $\Xi_{\text{solid}}^{(\theta_1)}, \Xi_{\text{crack}}^{(\theta_1)} \subset \mathbb{R}^3$  being the solid and crack phase of  $P_{\theta_1}$ , respectively. More precisely, it holds  
 317 that

$$\Xi_{\text{crack}}^{(\theta_1)} = \left\{ x \in \Xi_{\text{solid}}^{(\text{pr})} : \operatorname{dist}(x, f) \leq \frac{\delta}{2} \text{ for some } f \in C \right\}$$

318 and  $\Xi_{\text{solid}}^{(\theta_1)} = \Xi_{\text{solid}}^{(\text{pr})} \setminus \Xi_{\text{crack}}^{(\theta_1)}$ , where  $\operatorname{dist}(x, f) = \min\{|x - y| : y \in f\}$  denotes the Euclidean  
 319 distance from  $x \in \mathbb{R}^3$  to the set  $f \in C$ .

320 Note that the spatial orientation of the random crack depends solely on the initial facet  $f$ ,  
 321 which is chosen at random (uniformly) from the set of facets  $F$ . Since the orientation of a facet  
 322 of a Laguerre tessellation is uniformly distributed on the space of possible facet orientations, the  
 323 single crack model is isotropic. A potential anisotropy of the crack network could be modeled  
 324 by modifying the selection criterion formulated in Eq. (4).

325 **3.4. Crack network model.** Typically, the crack phase of particles observed in experimental  
 326 2D SEM data consists of more than one crack and forms complex crack networks, see Figure 1.

327 Thus, to model the crack phase of particles consisting of multiple cracks, we draw a realization  
 328  $n_{\text{cracks}} \in \mathbb{N} \cup \{0\}$  from a Poisson distributed random variable  $N_{\text{cracks}}$  with some parameter  
 329  $\lambda_P > 0$ . Furthermore, let  $P_{\theta_{1,1}}, \dots, P_{\theta_{1,n_{\text{cracks}}}}$  with  $P_{\theta_{1,i}} = (\Xi_{\text{solid}}^{(\theta_{1,i})}, \Xi_{\text{crack}}^{(\theta_{1,i})})$  for  $i = 1, \dots, n_{\text{cracks}}$   
 330 denote independent realizations of the single crack model introduced in Section 3.3, applied to  
 331 one and the same pristine particle  $P_{\text{pr}} = (\Xi_{\text{solid}}^{(\text{pr})}, \emptyset)$ . Overlaying these realizations results in a  
 332 realization of the crack network model  $P_{\theta_2} = (\Xi_{\text{solid}}^{(\theta_2)}, \Xi_{\text{crack}}^{(\theta_2)})$  with parameter vector

$$\theta_2 = (\theta_1, \lambda_P) = (\lambda_W, k_W, k_\Gamma, \theta_\Gamma, \lambda_P) \in \mathbb{R}_+^5, \quad (5)$$

333 where  $\Xi_{\text{crack}}^{(\theta_2)} = \bigcup_{i=1}^{n_{\text{cracks}}} \Xi_{\text{crack}}^{(\theta_1, i)}$  and  $\Xi_{\text{solid}}^{(\theta_2)} = \Xi_{\text{solid}}^{(\text{pr})} \setminus \Xi_{\text{crack}}^{(\theta_2)}$ .

334 By visual inspection of the SEM data, see Figure 1, it is obvious that the distributions of  
 335 the random number  $N_{\text{cracks}}$  and size  $N_{\text{facets}}$  of individual cracks should depend on the size of  
 336 the underlying pristine particle  $P_{\text{pr}}$ , i.e., small particles tend to have less and shorter cracks,  
 337 whereas large particles exhibit more and longer cracks. Therefore, we assume that the scale  
 338 parameters  $\lambda_{\text{P}}, \lambda_{\text{W}} > 0$  considered in Eq. (5) are given by

$$\lambda_{\text{P}} = \lambda_{\text{P}}(c_{\text{P}}, c_{\text{dim}}) = c_{\text{P}} \nu_3(\Xi_{\text{solid}}^{(\text{pr})})^{c_{\text{dim}}}, \quad \lambda_{\text{W}} = \lambda_{\text{W}}(c_{\text{W}}, c_{\text{dim}}) = c_{\text{W}} \nu_3(\Xi_{\text{solid}}^{(\text{pr})})^{1-c_{\text{dim}}} \quad (6)$$

339 for some constants  $c_{\text{P}}, c_{\text{W}} > 0$  and  $c_{\text{dim}} \in [0, 1]$ , where  $\nu_3$  denotes the 3-dimensional Lebesgue  
 340 measure, i.e.,  $\nu_3(\Xi_{\text{solid}}^{(\text{pr})})$  is the volume of  $P_{\text{pr}}$ . This implies that the porosity

$$p = \frac{\mathbb{E} \nu_3(\Xi_{\text{crack}}^{(\theta_2)})}{\nu_3(\Xi_{\text{solid}}^{(\text{pr})})},$$

341 of the crack network model  $P_{\theta_2}$  does not (or only slightly) depend on the volume  $\nu_3(\Xi_{\text{solid}}^{(\text{pr})})$  of  
 342 the underlying pristine particle  $P_{\text{pr}}$ , which can be shown as follows. Since the random variables  
 343  $N_{\text{cracks}}, N_{\text{facets}}, \Delta$  are assumed to be independent, it holds that<sup>3</sup>

$$p = \frac{\mathbb{E} \nu_3(\Xi_{\text{crack}}^{(\theta_2)})}{\nu_3(\Xi_{\text{solid}}^{(\text{pr})})} \approx \frac{\alpha \mathbb{E} N_{\text{cracks}} \mathbb{E} N_{\text{facets}} \mathbb{E} \Delta}{\nu_3(\Xi_{\text{solid}}^{(\text{pr})})} = \frac{\alpha \lambda_{\text{P}} \lambda_{\text{W}} \gamma_{k_{\text{W}}} \mathbb{E} \Delta}{\nu_3(\Xi_{\text{solid}}^{(\text{pr})})}, \quad (7)$$

344 where  $\alpha > 0$  is the mean area of planar facets of the Laguerre tessellation describing the grain  
 345 architecture of  $P_{\text{pr}}$  and  $\gamma_{k_{\text{W}}} = \Gamma(1 + \frac{1}{k_{\text{W}}})$  with the Gamma function  $\Gamma: (0, \infty) \mapsto \mathbb{R}_+$  given by  
 346  $\Gamma(x) = \int_0^\infty t^{x-1} e^{-t} dt$ . Thus, inserting Eq. (6) into Eq. (7), we get that

$$\begin{aligned} p &\approx \frac{\alpha c_{\text{P}} \nu_3(\Xi_{\text{solid}}^{(\text{pr})})^{c_{\text{dim}}} c_{\text{W}} \nu_3(\Xi_{\text{solid}}^{(\text{pr})})^{1-c_{\text{dim}}} \gamma_{k_{\text{W}}} \mathbb{E} \Delta}{\nu_3(\Xi_{\text{solid}}^{(\text{pr})})} \\ &= \nu_3(\Xi_{\text{solid}}^{(\text{pr})}) \frac{\alpha c_{\text{P}} c_{\text{W}} \gamma_{k_{\text{W}}} \mathbb{E} \Delta}{\nu_3(\Xi_{\text{solid}}^{(\text{pr})})} = \alpha c_{\text{P}} c_{\text{W}} \gamma_{k_{\text{W}}} \mathbb{E} \Delta, \end{aligned}$$

347 i.e., the porosity  $p$  of the crack network model  $P_{\theta_2}$  does not (or only slightly) depend on the  
 348 volume  $\nu_3(\Xi_{\text{solid}}^{(\text{pr})})$  of the underlying pristine particle  $P_{\text{pr}}$ .

349 Finally, we remark that from now on, utilizing the representation of the scale parameters  $\lambda_{\text{P}}$   
 350 and  $\lambda_{\text{W}}$  introduced in Eq. (6), the following modified form of the parameter vector  $\theta_2$  of  $P_{\theta_2}$   
 351 given in Eq. (5) will be used:

$$\theta_2 = (c_{\text{W}}, k_{\text{W}}, k_{\Gamma}, \theta_{\Gamma}, c_{\text{P}}, c_{\text{dim}}) \in \mathbb{R}_+^5 \times [0, 1]. \quad (8)$$

352 **3.5. Extended crack network model.** Recall Section 2.3, where the set of experimentally  
 353 measured 2D SEM images  $\mathcal{G}$  was split into two classes,  $\mathcal{G}_{\text{short}}$  and  $\mathcal{G}_{\text{long}}$ , containing particle cross  
 354 sections showing either predominantly short or long cracks. Nevertheless, each crack network  
 355 exhibited on these cross sections, still consists of both, (relatively) short as well as (relatively)  
 356 long cracks, see Figure 2.

357 This is the reason why the crack network model that was introduced in Section 3.4 turns out  
 358 to be insufficiently flexible. Therefore, we extend this model by realizing it twice on the same  
 359 pristine particle  $P_{\text{pr}} = (\Xi_{\text{solid}}^{(\text{pr})}, \emptyset)$ , with two different parameter vectors

$$\theta_2^{(1)} = (c_{\text{W}}^{(1)}, k_{\text{W}}^{(1)}, k_{\Gamma}^{(1)}, \theta_{\Gamma}^{(1)}, c_{\text{P}}^{(1)}, c_{\text{dim}}^{(1)}) \quad \text{and} \quad \theta_2^{(2)} = (c_{\text{W}}^{(2)}, k_{\text{W}}^{(2)}, k_{\Gamma}^{(2)}, \theta_{\Gamma}^{(2)}, c_{\text{P}}^{(2)}, c_{\text{dim}}^{(2)}).$$

<sup>3</sup>Note that this approximation does not take the overlap of cracked facets into consideration.

360 In this way we obtain two independently cracked particles

$$P_{\theta_2^{(1)}} = (\Xi_{\text{solid}}^{(\theta_2^{(1)})}, \Xi_{\text{crack}}^{(\theta_2^{(1)})}) \quad \text{and} \quad P_{\theta_2^{(2)}} = (\Xi_{\text{solid}}^{(\theta_2^{(2)})}, \Xi_{\text{crack}}^{(\theta_2^{(2)})}),$$

361 which are used to get the extended crack network model  $P_\theta = (\Xi_{\text{solid}}^{(\theta)}, \Xi_{\text{crack}}^{(\theta)})$  with  $\theta = (\theta_2^{(1)}, \theta_2^{(2)})$ ,  
 362 exhibiting a sufficiently large variety of short and long cracks, where

$$\Xi_{\text{crack}}^{(\theta)} = \Xi_{\text{crack}}^{(\theta_2^{(1)})} \cup \Xi_{\text{crack}}^{(\theta_2^{(2)})} \quad \text{and} \quad \Xi_{\text{solid}}^{(\theta)} = \Xi_{\text{solid}}^{(\text{pr})} \setminus \Xi_{\text{crack}}^{(\theta)}. \quad (9)$$

363 By visual inspection of the segmented SEM data, see Figure 2, it seems clear that short  
 364 and long cracks exhibit similar thicknesses. This observation motivates a reduction of model  
 365 parameters by setting  $k_\Gamma = k_\Gamma^{(1)} = k_\Gamma^{(2)}$  and  $\theta_\Gamma = \theta_\Gamma^{(1)} = \theta_\Gamma^{(2)}$ . Furthermore, we assume that the  
 366 influence of the volume  $\nu_3(\Xi_{\text{solid}}^{(\text{pr})})$  of the underlying pristine particle  $P_{\text{pr}}$  on the distributions  
 367 of the number and size of cracks is the same for short and long cracks, i.e., we assume that  
 368  $c_{\text{dim}}^{(1)} = c_{\text{dim}}^{(2)} = c_{\text{dim}}$ . Thus, the number of model parameters is reduced from 12 to 9, leading to  
 369 the parameter vector

$$\theta = (c_W^{(1)}, k_W^{(1)}, c_P^{(1)}, c_W^{(2)}, k_W^{(2)}, c_P^{(2)}, k_\Gamma, \theta_\Gamma, c_{\text{dim}}) \in \mathbb{R}_+^8 \times [0, 1] \quad (10)$$

370 of the extended crack network model, where  $c_W^{(i)}, k_W^{(i)}$  control the length,  $c_P^{(i)}$  the number and  
 371  $k_\Gamma, \theta_\Gamma$  the thickness of cracks for  $i \in \{1, 2\}$ , whereas  $c_{\text{dim}}$  controls the influence of the volume  
 372  $\nu_3(\Xi_{\text{solid}}^{(\text{pr})})$  of  $P_{\text{pr}}$  on the distributions of the number and size of cracks.

373 It is important to note that the crack network model as well as the extended crack network  
 374 model inherit isotropy from the single crack model.

#### 4. MODEL CALIBRATION

375  
 376 The calibration of the extended crack network model proposed in Section 3.5 is organized  
 377 as follows. First, in Section 4.1, we formulate a minimization problem to determine optimal  
 378 values of the parameter vector  $\theta$  given in Eq. (10). For this, in Section 4.2, three different  
 379 geometric descriptors of image data are introduced. These geometric descriptors are used in  
 380 Section 4.3 to define a loss function, which measures the discrepancy between experimentally  
 381 imaged particle cross sections and those drawn from the crack network model. Finally, in Section  
 382 4.4, a numerical method is described for solving the minimization problem stated in Section 4.1.

383 **4.1. Minimization problem.** The extended crack network model parameters introduced in  
 384 Section 3.5 are separately fitted to both partitions,  $\mathcal{G}_{\text{short}}$  and  $\mathcal{G}_{\text{long}}$ , of the experimental data set  
 385  $\mathcal{G}$  considered in Section 2.3. Thus, the optimization of the parameter vector  $\theta$  given in Eq. (10)  
 386 is performed twice, for  $\mathcal{G}_{\text{short}}$  and  $\mathcal{G}_{\text{long}}$ , where the discrepancy between geometric descriptors  
 387 of experimental image data and simulated image data drawn from the extended crack network  
 388 model is minimized. Figures 4 and 5 illustrate cross section realizations of virtual particles  
 389 drawn from the extended crack network model fitted to  $\mathcal{G}_{\text{short}}$  and  $\mathcal{G}_{\text{long}}$ , respectively, alongside  
 390 experimentally imaged cross sections.

391 Furthermore, it is important to note that the crack network morphology may significantly  
 392 vary across different cross-section sizes, see Figure 1. To avoid systematic errors arising from  
 393 comparing experimental and simulated cross sections of different sizes, we introduce several  
 394 cross-section size classes. Thus, experimental and simulated cross-sections are only compared  
 395 if they are approximately of the same size. More specifically, a simulated particle cross-section  
 396 is compared to the average of all experimental cross-sections in the same size class.

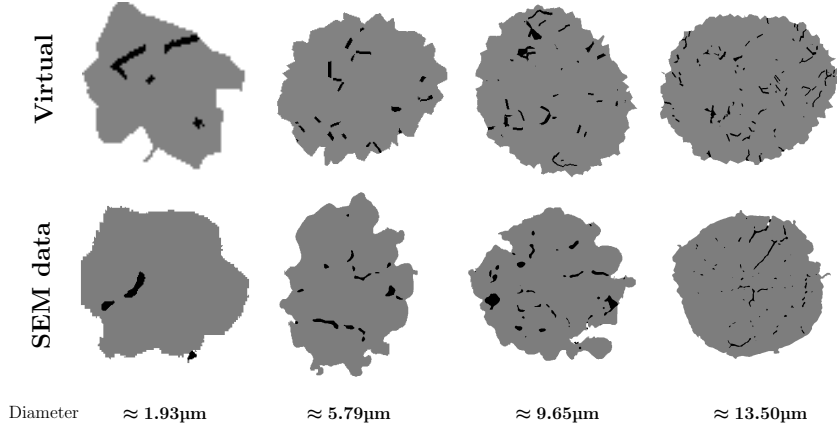


FIGURE 4. Particle cross sections across various size classes, drawn from the extended crack network model calibrated to  $\mathcal{G}_{\text{short}}$  (top row) and corresponding representatives of  $\mathcal{G}_{\text{short}}$  (bottom row). The cross sections were scaled to the same size, while their actual sizes are indicated by their area-equivalent diameters.

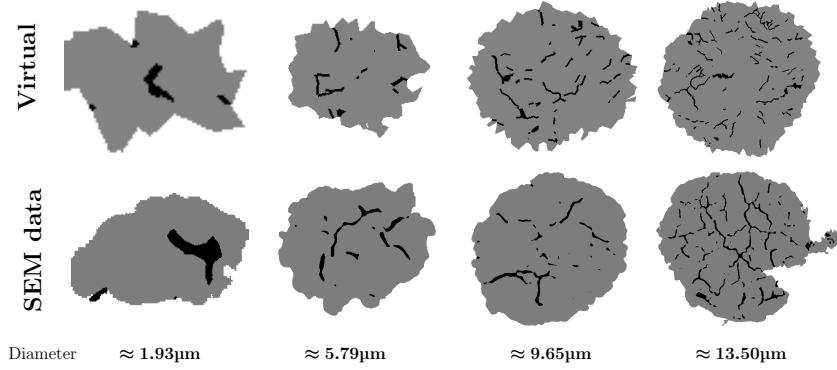


FIGURE 5. Particle cross sections across various size classes, drawn from the extended crack network model calibrated to  $\mathcal{G}_{\text{long}}$  (top row) and corresponding representatives of  $\mathcal{G}_{\text{long}}$  (bottom row). The cross sections were scaled to the same size, while their actual sizes are indicated by their area-equivalent diameters.

397 For the sake of simplicity, we will use the following abbreviating notation, writing  $\mathcal{G}$  instead of  
 398  $\mathcal{G}_{\text{short}}$  and  $\mathcal{G}_{\text{long}}$ . Furthermore, for each  $d > 0$ , let  $\mathcal{G}|_d$  be the restriction of  $\mathcal{G}$  to all particle cross  
 399 sections  $P_{\text{ex}}$  whose area-equivalent diameter  $\text{aed}(P_{\text{ex}})$  belongs to the interval  $B_\ell(d) = [j\ell, (j+1)\ell)$   
 400 with given length  $\ell > 0$ , where the integer  $j \in \mathbb{N} \cup \{0\}$  is chosen such that  $d \in [j\ell, (j+1)\ell)$ . It  
 401 turned out that an interval length of  $\ell \approx 1.29 \mu\text{m}$  balances a reasonable number of experimental  
 402 cross sections in each bin and, simultaneously, preserves a sufficiently fine subdivision of the  
 403 entire dataset  $\mathcal{G}$ , where this subdivision results into 11 size intervals  $[0, \ell), \dots, [10\ell, 11\ell)$ , with  
 404  $11\ell \approx 14.1 \mu\text{m}$ .<sup>4</sup> However, since the stochastic 3D model for pristine NMC particles, described  
 405 in Section 3.1, has been calibrated to 3D nano-CT data [50], it happens that for some randomly  
 406 oriented planes  $E \subset \mathbb{R}^2$ , the cross sections  $P_\theta \cap E$  of 3D particles drawn from the extended crack  
 407 network model  $P_\theta$  are larger than the ones observed in the dataset  $\mathcal{G}$ , which were measured by  
 408 the 2D SEM technique. Thus, if the area-equivalent diameter of  $P_\theta \cap E$  is larger than  $11\ell$ , which

<sup>4</sup>The interval length of  $\ell \approx 1.29 \mu\text{m}$  corresponds to approximately 90 pixels of the experimental data.

409 is the upper bound of the largest size class  $B_\ell(10)$  of the experimental data set  $\mathcal{G}$  (for both cases  
410  $\mathcal{G} = \mathcal{G}_{\text{short}}$  and  $\mathcal{G} = \mathcal{G}_{\text{long}}$ ), then  $P_\theta \cap E$  is not considered in the minimization procedure.

411 This leads to the minimization problem

$$\hat{\theta} = \underset{\theta \in \mathbb{R}_+^8 \times [0,1]}{\operatorname{argmin}} \quad \mathbb{E} L\left(P_\theta \cap E, \mathcal{G}|_{\operatorname{aed}(P_\theta \cap E)}\right), \quad (11)$$

412 where the expectation in Eq. (11) extends over cross sections  $P_\theta \cap E$  such that  $\operatorname{aed}(P_\theta \cap E) \leq 11\ell$ ,  
413 and  $L(\cdot, \cdot)$  is some loss function, which measures the discrepancy between the cross section  $P_\theta \cap E$   
414 of the extended crack network model  $P_\theta$  and particle cross sections belonging to the restriction  
415  $\mathcal{G}|_{\operatorname{aed}(P_\theta \cap E)}$  of  $\mathcal{G}$ .

416 **4.2. Geometric descriptors of 2D image data.** In this section, three different geometric  
417 descriptors of 2D image data are considered: the two-point coverage probability function, the  
418 crack-size distribution and the distance-to-background distribution. They will be determined  
419 on (measured and simulated) particle cross sections, denoted by  $P = (\Xi_{\text{solid}}, \Xi_{\text{crack}})$ , where  
420  $\Xi_{\text{solid}}, \Xi_{\text{crack}} \subset \mathbb{R}^2$ . Furthermore, these descriptors will be employed in Section 4.3 to determine  
421 the loss function considered in Eq. (11).

422 Since the extended crack model is isotropic, we did not consider structural descriptors of  
423 generated crack networks that could take directional dependencies into account.

424 **Two-point coverage probability.** For each  $h \in [0, h_{\text{max}}]$ , where  $h_{\text{max}} > 0$  is some maxi-  
425 mum distance, the so-called the two-point coverage probability, denoted by  $\operatorname{prob}_\Xi(h)$ , is the  
426 probability that two randomly chosen points  $x_1, x_2 \in \Xi_{\text{solid}} \cup \Xi_{\text{crack}}$  of distance  $h$  belong to  
427 the particle phase  $\Xi \in \{\Xi_{\text{solid}}, \Xi_{\text{crack}}\}$ . This probability will be estimated by the number of  
428 pixel pairs  $x_1, x_2 \in \Xi \cap \mathbb{Z}_\rho^2$  separated by distance  $h$ , divided by the total number of pixel pairs  
429  $x_1, x_2 \in (\Xi_{\text{solid}} \cup \Xi_{\text{crack}}) \cap \mathbb{Z}_\rho^2$  of distance  $h$ , i.e.,

$$\operatorname{prob}_\Xi(h) \approx \frac{\#\{x_1, x_2 \in \Xi \cap \mathbb{Z}_\rho^2: |x_1 - x_2| = h\}}{\#\{x_1, x_2 \in (\Xi_{\text{solid}} \cup \Xi_{\text{crack}}) \cap \mathbb{Z}_\rho^2: |x_1 - x_2| = h\}},$$

430 where  $|\cdot|$  denotes the Euclidean norm in  $\mathbb{R}^2$ , see e.g., [67] for further details.

431 For the data considered in the present paper, the two-point coverage probabilities  $\operatorname{prob}_{\Xi_{\text{solid}}}(h)$   
432 and  $\operatorname{prob}_{\Xi_{\text{crack}}}(h)$  are estimated for all possible distances  $h \in [0, h_{\text{max}}]$  on the pixel grid, where  
433  $h_{\text{max}} \approx 850$  nm, because it turned out that the values obtained for  $\operatorname{prob}_{\Xi_{\text{solid}}}(h)$  and  $\operatorname{prob}_{\Xi_{\text{crack}}}(h)$   
434 are typically constant for  $h > 850$  nm. These probabilities are then interpolated utilizing cubic  
435 splines and evaluated for 30 equidistant values of  $h$ , corresponding to a step size of approximately  
436 28 nm, which leads to the vectors of relative frequencies

$$\operatorname{prob}_{\text{solid}}(P) = (\operatorname{prob}_{\Xi_{\text{solid}}}(h_0), \operatorname{prob}_{\Xi_{\text{solid}}}(h_1), \dots, \operatorname{prob}_{\Xi_{\text{solid}}}(h_{29})) \in [0, 1]^{30} \quad (12)$$

437 and

$$\operatorname{prob}_{\text{crack}}(P) = (\operatorname{prob}_{\Xi_{\text{crack}}}(h_0), \operatorname{prob}_{\Xi_{\text{crack}}}(h_1), \dots, \operatorname{prob}_{\Xi_{\text{crack}}}(h_{29})) \in [0, 1]^{30}, \quad (13)$$

438 where  $h_i = i h_{\text{max}}/29$  for  $i = 0, 1, \dots, 29$ .

439 **Crack-size distribution.** The probability distribution of the size of a randomly chosen crack  
440 within a particle cross section  $P = (\Xi_{\text{solid}}, \Xi_{\text{crack}})$  will also be incorporated into the loss function  
441 introduced in Eq. (11). Formally, a crack is considered to be a connected component of the  
442 crack phase  $\Xi_{\text{crack}}$ , where the crack size will be represented by the area-equivalent diameter of  
443 the crack.

444 Recall that  $\text{aed}(\xi)$  denotes the area-equivalent diameter of a set  $\xi \subset \mathbb{R}^2$ . Furthermore, let  
 445  $\xi_1, \dots, \xi_n \subset \Xi_{\text{crack}}$  denote the connected components of the crack phase  $\Xi_{\text{crack}}$ . The probability  
 446 density of the random crack size will then be estimated by a histogram with some bin width  
 447  $w > 0$ , which is given by the relative frequencies

$$\text{prob}_{\text{size}}(k) = \frac{\#\{\xi \in \{\xi_1, \dots, \xi_n\} : \text{aed}(\xi) \in [kw, (k+1)w)\}}{n}$$

448 for  $k = 0, 1, \dots, 49$ , where we put  $w = 50$  nm. Altogether, this leads to the vector of relative  
 449 frequencies  $\text{prob}_{\text{size}}(P) = (\text{prob}_{\text{size}}(0), \text{prob}_{\text{size}}(1), \dots, \text{prob}_{\text{size}}(49)) \in [0, 1]^{50}$ .

450 **Distance-to-background distribution.** Consider a randomly chosen point  $X \in \Xi_{\text{crack}}$  within  
 451 the crack phase  $\Xi_{\text{crack}}$  of a particle cross section  $P = (\Xi_{\text{solid}}, \Xi_{\text{crack}})$ , and the random (minimum)  
 452 distance  $D$  from  $X$  to the background  $\mathbb{R}^2 \setminus (\Xi_{\text{solid}} \cup \Xi_{\text{crack}})$  surrounding  $P$ , i.e.,

$$D = \min\{|X - y| : y \in \mathbb{R}^2 \setminus (\Xi_{\text{solid}} \cup \Xi_{\text{crack}})\}.$$

453 The probability distribution of the random variable  $D$  will be taken into account as a third  
 454 component in the loss function introduced in Eq. (11). Like for the crack sizes considered  
 455 above, the probability density of  $D$  will be estimated by a histogram with some bin width  
 456  $w > 0$ , which is specified by the relative frequencies

$$\text{prob}_{\text{dist}}(k) = \frac{\#\{x \in \Xi_{\text{crack}} \cap \mathbb{Z}_\rho^2 : \min\{|x - y| : y \in \mathbb{R}^2 \setminus (\Xi_{\text{solid}} \cup \Xi_{\text{crack}})\} \in [kw, (k+1)w)\}}{\#\Xi_{\text{crack}} \cap \mathbb{Z}_\rho^2}$$

457 for  $k = 0, 1, \dots, 119$ , where we put  $w = 50$  nm. In summary, we obtain the vector of relative  
 458 frequencies  $\text{prob}_{\text{dist}}(P) = (\text{prob}_{\text{dist}}(0), \text{prob}_{\text{dist}}(1), \dots, \text{prob}_{\text{dist}}(119)) \in [0, 1]^{120}$ .

459 **4.3. Loss function.** We now specify the loss function  $L(\cdot, \cdot)$  considered in Eq. (11), utilizing  
 460 the geometric particle descriptors stated in Section 4.2. Recall that the purpose of the loss  
 461 function is to measure the discrepancy between experimentally imaged particle cross sections  
 462 and those drawn from the extended crack network model stated in Section 3.5. In particular,  
 463 the loss function will be utilized in Section 4.4 to solve the minimization problem introduced in  
 464 Eq. (11).

465 Let  $\mathcal{G}$  denote some set of experimentally imaged particle cross sections, e.g.  $\mathcal{G} = \mathcal{G}_{\text{short}}$ .  
 466 Furthermore, let

$$\overline{\text{prob}}_{\text{solid}}(\mathcal{G}) = \frac{1}{\#\mathcal{G}} \sum_{P=(\Xi_{\text{solid}}, \Xi_{\text{crack}}) \in \mathcal{G}} \text{prob}_{\text{solid}}(P).$$

467 be the componentwise average of the vector of relative frequencies given in Eq. (12). The aver-  
 468 ages  $\overline{\text{prob}}_{\text{crack}}(\mathcal{G})$ ,  $\overline{\text{prob}}_{\text{size}}(\mathcal{G})$  and  $\overline{\text{prob}}_{\text{dist}}(\mathcal{G})$  for the two-point coverage probability of the crack  
 469 phase, crack-size distribution and distance-to-background distribution are defined analogously.  
 470 The loss function considered in Eq. (11) is then given by

$$\begin{aligned} L(P_\theta \cap E, \mathcal{G}|_{\text{aed}(P_\theta)}) &= \text{error}\left(\text{prob}_{\text{crack}}(P_\theta \cap E), \overline{\text{prob}}_{\text{crack}}(\mathcal{G}|_{\text{aed}(P_\theta \cap E)})\right) \\ &\quad + \text{error}\left(\text{prob}_{\text{solid}}(P_\theta \cap E), \overline{\text{prob}}_{\text{solid}}(\mathcal{G}|_{\text{aed}(P_\theta \cap E)})\right) \\ &\quad + \text{error}\left(\text{prob}_{\text{size}}(P_\theta \cap E), \overline{\text{prob}}_{\text{size}}(\mathcal{G}|_{\text{aed}(P_\theta \cap E)})\right) \\ &\quad + \text{error}\left(\text{prob}_{\text{dist}}(P_\theta \cap E), \overline{\text{prob}}_{\text{dist}}(\mathcal{G}|_{\text{aed}(P_\theta \cap E)})\right), \end{aligned}$$

471 where  $\text{error}(\cdot, \cdot)$  is an error function which quantifies the discrepancy between a random cross  
 472 section  $P_\theta \cap E$  of the extended crack network model  $P_\theta$ , and the set  $\mathcal{G}|_{\text{aed}(P_\theta \cap E)}$  of experimentally  
 473 imaged cross sections. More precisely, we consider the truncated mean absolute error

$$\text{error}(x, y) = \frac{1}{n_+} \sum_{i=1}^{n_+} |x_i - y_i| \quad (14)$$

474 for  $x = (x_1, \dots, x_n), y = (y_1, \dots, y_n) \in \mathbb{R}^n$ , where  $n_+ \leq n$  is the smallest integer  $j \in \{1, \dots, n\}$   
 475 such that  $x_i = y_i = 0$  for all  $i \in \{j + 1, \dots, n\}$ .

476 Note that truncating the sum in Eq. (14) at  $n_+ \leq n$  is motivated by the fact that the  
 477 components of the vectors of relative frequencies considered in Section 4.2 are equal to zero from  
 478 a certain index. For the two-point coverage probabilities  $\text{prob}_{\text{solid}}(\cdot)$  and  $\text{prob}_{\text{crack}}(\cdot)$  occurring  
 479 in Eqs. (12) and (13), respectively, this happens when the size of the particle cross section is  
 480 smaller than  $h_{\text{max}} \approx 850$  nm. Furthermore, for  $\text{prob}_{\text{size}}(\cdot)$  and  $\text{prob}_{\text{dist}}(\cdot)$ , some cross sections  
 481 may contain only features smaller than a certain threshold. Truncating the sum in Eq. (14)  
 482 ensures that the sum of absolute values of the right-hand side of Eq. (14) is normalized with the  
 483 actual number of non-zero components of both vectors  $x, y \in \mathbb{R}^n$ . Thus, this approach prevents  
 484 that the error considered in Eq. (14) is not appropriately weighted, which could occur if many  
 485 components of  $x, y \in \mathbb{R}^n$  are equal to zero.

486 **4.4. Numerical solution of the minimization problem.** For solving the minimization  
 487 problem stated in Eq. (11), a Nelder-Mead approach [69] is utilized, where a Monte Carlo  
 488 simulation technique [70] is employed in each iteration step of the Nelder-Mead algorithm to  
 489 approximate the expected value of the loss  $L(P_\theta \cap E, \mathcal{G}|_{\text{aed}(P_\theta)})$ .

490 This process involves averaging over numerous cross sections  $P_\theta^{(i)} \cap E^{(i)}$ , where  $P_\theta^{(i)}$  is a  
 491 realization of the extended crack network model  $P_\theta$ , and  $E^{(i)}$  is a realization of the randomly  
 492 orientated plane  $E \subset \mathbb{R}^3$  for each  $i = 1, \dots, n$  and some integer  $n \in \mathbb{N}$ . Recall that  $P_\theta$  is  
 493 an isotropic model, i.e., the realizations of  $P_\theta$  exhibit a statistically similar behavior in each  
 494 direction. Thus, it would be sufficient, to intersect each realization  $P_\theta^{(i)}$  of  $P_\theta$  with a single plane  
 495  $E_{x,v} \subset \mathbb{R}^3$ , where  $E_{x,v}$  denotes a plane that is orthogonal to the x-axis and has a certain distance  
 496  $v > 0$  from the origin  $o \in \mathbb{R}^3$ . However, to keep the computational effort low and, simultaneously,  
 497 increase the robustness of averaging, each realization  $P_\theta^{(i)}$  is intersected at multiple distances  
 498 along the x-, y- and z- axis, respectively. Furthermore, to avoid interpolations of the pixelized  
 499 image data, cross sections are only taken at integer heights along the coordinate axes.

500 First, 100 pristine particles are drawn from the stochastic 3D model for polycrystalline NMC  
 501 particles, which has been described in Section 3.1. Then, in each iteration step of the Nelder-  
 502 Mead minimization algorithm, 32 out of these 100 particles, denoted by  $P_{\text{pr}}^{(i)} = (\Xi_{\text{solid}}^{(\text{pr}, i)}, \emptyset)$  for  
 503  $i = 1, \dots, 32$ , are chosen with a probability proportional to their volume-equivalent diameter.  
 504 Note that this selection method corresponds to the probability of intersecting a particle by a  
 505 randomly chosen plane, as this is done in 2D SEM imaging [71].

506 Each pristine particle  $P_{\text{pr}}^{(i)}$  serves as input for generating a realization of the extended crack  
 507 network model  $P_\theta$ , which results in 32 realizations of  $P_\theta$ , denoted by  $P_\theta^{(i)} = (\Xi_{\text{solid}}^{(\theta, i)}, \Xi_{\text{crack}}^{(\theta, i)})$  for  
 508  $i = 1, \dots, 32$ . Additionally, for each realization  $P_\theta^{(i)}$ , multiple cross sections are generated by  
 509 intersecting each simulated particle  $P_\theta^{(i)}$  at 10%, 20%, ..., 90% of its size along the x-, y- and  
 510 z-axis, respectively. This yields 32 realizations of  $P_\theta$ , each sliced at 9 positions along 3 axes,  
 511 which finally results into  $32 \times 9 \times 3 = 864$  cross sections per iteration step.

512 More formally, for each simulated particle  $P_\theta^{(i)}$ , we assume without loss of generality that it  
 513 is located in the positive octant  $\mathbb{R}_+^3 = [0, \infty)^3 \subset \mathbb{R}^3$  and touches the xy-plane, xz-plane and  
 514 yz-plane. Furthermore, let  $\text{diam}_x(P_\theta^{(i)})$  denote the Feret diameter of  $P_\theta^{(i)}$  [72] along the x-axis,  
 515 which is given by

$$\text{diam}_x(P_\theta^{(i)}) = \max\left\{v > 0: (\Xi_{\text{solid}}^{(\theta,i)} \cup \Xi_{\text{crack}}^{(\theta,i)}) \cap E_{x,v} \neq \emptyset\right\}, \quad (15)$$

516 i.e.,  $\text{diam}_x(P_\theta^{(i)})$  describes the size of  $P_\theta^{(i)}$  in x-direction. Analogously, the Feret diameters of  
 517  $P_\theta^{(i)}$  along the y- and z- axis will be denoted by  $\text{diam}_y(P_\theta^{(i)})$  and  $\text{diam}_z(P_\theta^{(i)})$ , where the plane  
 518  $E_{x,v}$  on the right-hand side of Eq. (15) is replaced by planes  $E_{y,v}$  and  $E_{z,v} \in \mathbb{R}^3$  that are  
 519 orthogonal to the y- and z-axis, respectively, and have the distance  $v > 0$  to the origin.

520 Then, the expected loss  $\mathbb{E} L(P_\theta \cap E, \mathcal{G}|_{\text{aed}(P_\theta)})$ , occurring in Eq. (11), is numerically approx-  
 521 imated by

$$\mathbb{E} L\left(P_\theta \cap E, \mathcal{G}|_{\text{aed}(P_\theta \cap E)}\right) \approx \frac{1}{864} \sum_{i=1}^{32} \sum_{a \in \{x,y,z\}} \sum_{j=1}^9 L\left(P_\theta^{(i)} \cap E(a, j, P_\theta^{(i)}), \mathcal{G}|_{\text{aed}(P_\theta^{(i)} \cap E(a, j, P_\theta^{(i)}))}\right)$$

522 where  $E(a, j, P) = E_{a, \text{round}(j/10 \cdot \text{diam}_a(P))}$  and  $\text{round}(\cdot)$  denotes rounding to the closest integer,  
 523 as defined in Eq. (3).

524 Thus, in summary, to find the optimal parameter vector  $\hat{\theta}$  which solves the minimization  
 525 problem given in Eq. (11), in each iteration step of the Nelder-Mead algorithm we choose 32  
 526 pristine particles out of a pool of 100 realizations of the stochastic 3D model described in  
 527 Section 3.1. These selected particles serve as input for the extended crack network model  $P_\theta$ ,  
 528 where the expected loss is approximated by averaging over 864 cross sections.

529 Recall that the optimization procedure described above was separately applied to both data  
 530 sets,  $\mathcal{G}_{\text{short}}$  and  $\mathcal{G}_{\text{long}}$ , resulting in two calibrated models which generate particles exhibiting  
 531 predominately short or long cracks. In the following, we will refer to the extended crack network  
 532 model calibrated to  $\mathcal{G}_{\text{short}}$  and  $\mathcal{G}_{\text{long}}$  as  $P_{\hat{\theta}_{\text{short}}}$  and  $P_{\hat{\theta}_{\text{long}}}$ , where samples drawn from these two  
 533 models are called short- and long-cracked particles, respectively.

## 534 5. RESULTS AND DISCUSSION

535 In this section we first show how the extended crack network model  $P_{\hat{\theta}}$  can be validated, the  
 536 calibration of which to experimental data has been explained in Section 4. For this, further  
 537 geometric descriptors of 2D morphologies will be introduced in Section 5.1, which have not  
 538 been used for model calibration. Then, similarly to the model calibration approach considered  
 539 in Section 4, the distributions of these descriptors will be determined in Section 5.2 for simulated  
 540 2D cross sections, drawn from  $P_{\hat{\theta}}$ , and compared to those computed for experimental 2D SEM  
 541 data. Moreover, in Section 5.3, two transport-relevant particle descriptors are presented, which  
 542 influence the performance of Li-ion batteries, but can only be determined adequately if 3D data  
 543 is available. In Section 5.4, the distributions of these transport-relevant descriptors, namely the  
 544 relative shortest path length of Li transport in active material, as well as the relative specific  
 545 surface area of active material, are analyzed for simulated (pristine and cracked) 3D particles.

546 **5.1. Additional geometric descriptors of 2D morphologies.** For validating the goodness  
 547 of model fit, six further descriptors of 2D morphologies are taken into account to compare planar  
 548 cross-sections of the extended crack network model  $P_{\hat{\theta}}$  to experimentally measured 2D SEM  
 549 images described in Section 2. It is important to emphasize that the descriptors considered in the  
 550 present section are not used during the calibration process explained in Section 4. Furthermore,

551 note that these descriptors are defined for planar particle cross-sections  $P = (\Xi_{\text{solid}}, \Xi_{\text{crack}})$ ,  
 552 with  $\Xi_{\text{solid}}, \Xi_{\text{crack}} \subset \mathbb{R}^2$ , which are either the continuous representation of an experimentally  
 553 measured particle cross-section, or derived by intersecting a simulated cracked 3D particle,  
 554 drawn from  $P_{\hat{\theta}}$ , with a randomly oriented plane  $E \subset \mathbb{R}^3$ .

555 **Porosity.** One of the most fundamental geometric descriptors of porous 2D morphologies is  
 556 their porosity. In the case of a planar particle cross sections  $P = (\Xi_{\text{solid}}, \Xi_{\text{crack}})$ , the porosity  
 557  $p \in [0, 1]$  can be given by

$$p = \frac{\nu_2(\Xi_{\text{crack}})}{\nu_2(\Xi_{\text{solid}} \cup \Xi_{\text{crack}})},$$

558 see also Eq.(7) in Section 3.4, where the porosity was assumed to be independent of the particle  
 559 size. However, recall that the porosity was not used in Section 4 for calibrating the extended  
 560 crack network model  $P_{\hat{\theta}}$  to experimental data. In Section 5.2 we determine the (empirical) di-  
 561 stribution of  $p$  for simulated 2D cross sections, drawn from  $P_{\hat{\theta}}$ , and compare it to that computed  
 562 for experimental 2D SEM data.

563 **Chord length.** Let  $v \in \{x \in \mathbb{R}^2 : |x| = 1\}$  be some predefined direction in  $\mathbb{R}^2$ . Then,  
 564 chords within the solid phase  $\Xi_{\text{solid}}$  can be obtained by intersecting  $\Xi_{\text{solid}}$  with (parallel) lines in  
 565 direction  $v$ . In general, this intersection results in multiple line segments, which are referred to  
 566 as chords, see Figure 6a for chords in y-direction, i.e.,  $v = (0, 1)$ . The probability distribution  
 567 of the lengths of these line segments is called chord length distribution. Under the assumption  
 568 of isotropy, the chord length distribution does not depend on the chosen direction  $v$ , see [67] for  
 569 formal definitions.

570 For 2D SEM data the chord length distribution was estimated by considering chords in x- and  
 571 y-direction. However, for simulated 3D particles, drawn from  $P_{\hat{\theta}}$ , chords along the z-direction  
 572 were additionally taken into account, which increases robustness of the estimation. For the  
 573 computation of chord lengths, the python package PoreSpy [73] was used.

574 **Local entropy.** The mean local entropy of a particle cross section  $P = (\Xi_{\text{solid}}, \Xi_{\text{crack}})$  is a  
 575 measure for the local heterogeneity of  $P$ . It can be defined in the by the following: First, assign  
 576 each point  $x = (x_1, x_2) \in \Xi_{\text{solid}} \cup \Xi_{\text{crack}} \subset \mathbb{R}^2$  its local entropy

$$E(x) = - \sum_{\Xi \in \{\Xi_{\text{solid}}, \Xi_{\text{crack}}\}} \varepsilon_{\Xi}(x) \log_2(\varepsilon_{\Xi}(x))$$

577 where  $\varepsilon_{\Xi}(x) \in [0, 1]$  denotes the local volume fraction of phase  $\Xi \in \{\Xi_{\text{solid}}, \Xi_{\text{crack}}\}$ , Note that  
 578  $\varepsilon_{\Xi}(x)$  is determined by means of the  $15 \times 15$  neighborhood  $K_{15}(x) \subset \mathbb{R}^2$  centered iat  $x \in$   
 579  $\Xi_{\text{solid}} \cup \Xi_{\text{crack}}$ , and formally given by

$$\varepsilon_{\Xi}(x) = \frac{\nu_2(\Xi \cap K_{15}(x))}{\nu_2(\Xi_{\text{solid}} \cup \Xi_{\text{crack}} \cap K_{15}(x))}, \quad (16)$$

580 where  $K_{15}(x) = \{y = (y_1, y_2) \in \mathbb{R}^2 : |x - y| \leq 15\}$  with  $|x - y| = |x_1 - y_1| + |x_2 - y_2|$ , being  
 581 the so-called Manhattan metric. Then, the mean local entropy of the particle cross section  
 582  $P = (\Xi_{\text{solid}}, \Xi_{\text{crack}})$  is given by

$$E(P) = \frac{1}{\nu_2(\Xi_{\text{solid}} \cup \Xi_{\text{crack}})} \int_{\Xi_{\text{solid}}, \Xi_{\text{crack}}} E(x) dx, \quad (17)$$

583 i.e., by averaging the local entropy  $E(x)$  over all  $x \in \Xi_{\text{solid}} \cup \Xi_{\text{crack}}$  belonging either to the crack  
 584 or solid phase.

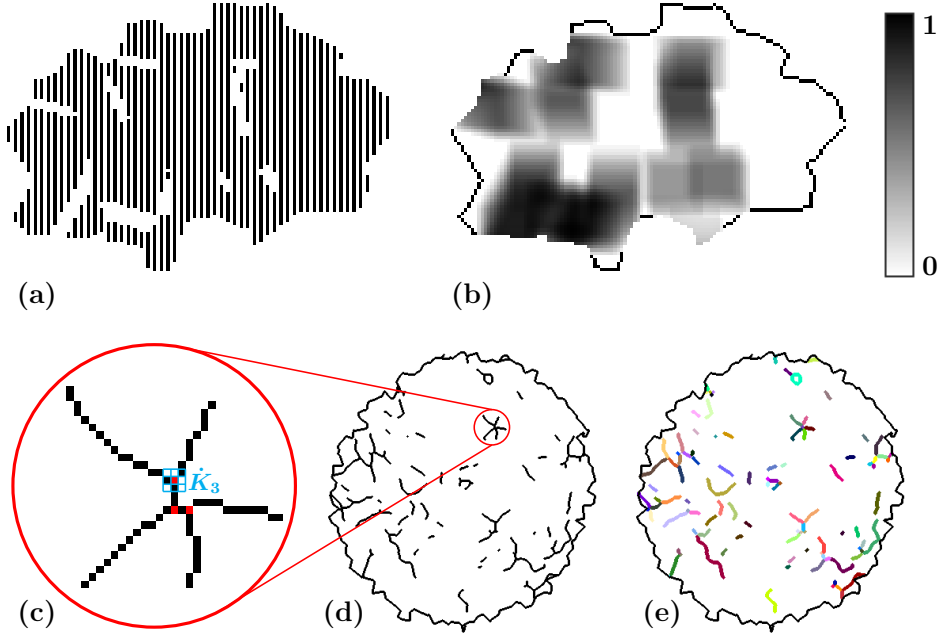


FIGURE 6. Geometric descriptors of 2D morphologies, including chord lengths (a) and local entropy (b) of an elongated particle, as well as the number of branching points within a magnified region (c) of a skeletonized crack network (d), along with the number and length of crack segments (e) in another, more spherical particle. Note that for illustrative purposes, the skeletons in (d) and (e) are dilated and the grain boundaries in (b), (d) and (e) are indicated.

585 In Section 5.2, the distribution of the mean local entropy  $E(P)$  given in Eq. (17) will be  
 586 estimated for 2D image data and, therefore, the local entropy  $\varepsilon_{\Xi}(x)$  introduced in (16) will  
 587 be determined pixelwise. However, note that the latter quantity is highly sensitive to changes  
 588 of resolution, because a finer resolution corresponds to a kernel  $K_{15}$  containing more pixels to  
 589 cover a predefined area, potentially resulting in a higher local heterogeneity. Therefore, the  
 590 experimental 2D SEM data were downsampled to match the (coarser) resolution of the virtual  
 591 pristine particles drawn from the stochastic 3D model, as described in Section 3.1. Figure 6b  
 592 illustrates a visual impression of local entropy computed on pixelized image data.

593 **Number of branching points.** To investigate the branching behavior of the crack phase  $\Xi_{\text{crack}}$   
 594 of a particle cross section  $P = (\Xi_{\text{solid}}, \Xi_{\text{crack}})$ , we consider its skeleton, denoted by  $\mathcal{S}(P)$ , see  
 595 also Section 2.3. Recall that in Section 2.3, each connected component of the crack phase has  
 596 been represented by its center line, called skeleton segment and denoted by  $S \in \mathcal{S}(P)$ , where the  
 597 family of all skeleton segments forms the skeleton. In the following, for each skeleton segment  
 598  $S \in \mathcal{S}(P)$ , we say that  $x \in S$  is a branching point if there are at least three points  $y_1, y_2, y_3 \in S$   
 599 such that  $|x - y_i| = \varepsilon$ , where the set  $\varepsilon > 0$  is a sufficient small distance.

600 To estimate the distribution of the number of branching points from pixelized image data,  
 601 for any  $S \in \mathcal{S}(P)$  and  $x \in S \cap \mathbb{Z}_{\rho}^2$ , let  $\dot{K}_3(x) = (K_3(x) \cap \mathbb{Z}_{\rho}^2) \setminus \{x\}$  denote the  $3 \times 3$  neighborhood  
 602 of  $x$  on the grid  $\mathbb{Z}_{\rho}^2$ , excluding the point  $x$  itself. A point  $x \in S \cap \mathbb{Z}_{\rho}^2$  is considered a branching  
 603 point if  $\#(S \cap \dot{K}_3(x)) \geq 3$ , see Figure 6c, where  $\dot{K}_3(x)$  is visualized in blue color.

604 The python package PlantCV has been used [74] to compute skeleton segments and branching  
 605 points.

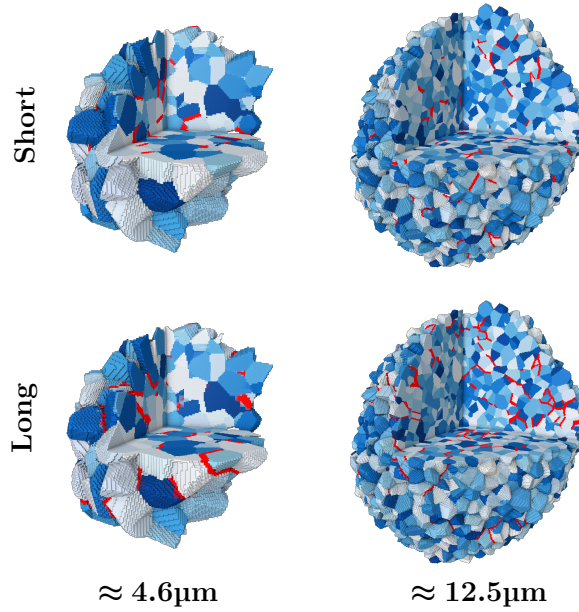


FIGURE 7. Exemplary clipped 3D renderings of virtually generated cracked NMC particles, drawn from the extended crack network model. Cracks are indicated in red color, whereas individual grains are visualized in randomly chosen shades of blue. The top row, shows particles drawn from the extended crack model calibrated to  $\mathcal{G}_{\text{short}}$ , whereas the bottom row corresponds to  $\mathcal{G}_{\text{long}}$ . The left column features a particle with a volume-equivalent diameter of  $\approx 4.6 \mu\text{m}$ , while the right column shows one of  $\approx 12.5 \mu\text{m}$ .

606 **Number and length of crack segments.** By removing the branching points from a skeleton  
 607 segment  $S \subset \mathcal{S}(P)$ , we obtain various connected components of  $S$  which we refer to as crack  
 608 segments, see Figure 6e, where crack segments are indicated in different colors. Furthermore,  
 609 for validation of the fitted extended crack network model  $P_{\hat{\theta}}$ , we determine the distributions  
 610 of the number and length of crack segments for simulated 2D cross sections, drawn from  $P_{\hat{\theta}}$ ,  
 611 and compare them to those computed for experimental 2D SEM data. Note that the notion of  
 612 crack segment length introduced in this section is different from that of crack size, which was  
 613 considered in Sections 4.2 to 4.4 for model fitting.

614 **5.2. Model validation.** To validate the extended crack network model, which has been cali-  
 615 brated to experimental image data in Sections 4.2 to 4.4, the probability densities of the geo-  
 616 metric descriptors stated in Section 5.1 are estimated using particle cross sections of 200 model  
 617 realizations drawn from each of the extended crack models  $P_{\hat{\theta}_{\text{short}}}$  and  $P_{\hat{\theta}_{\text{long}}}$ . For a visual  
 618 impression of realizations of the fitted model, we refer to Figure 7, which presents clipped 3D  
 619 renderings of virtually generated cracked NMC particles. To ensure comparability, only 2D cross  
 620 sections of the 3D realizations have been taken into account, which are extracted, similarly as  
 621 described in Section 4.4, at 10%, 20%,  $\dots$ , 90% of the particle size along x-, y- and z-direction,  
 622 resulting into  $9 \cdot 3 \cdot 200 = 5400$  cross sections for both crack scenarios. For each of these cross  
 623 sections, the porosity, mean local entropy, number of branching points, as well as the number  
 624 and length of crack segments are determined. Their probability densities, along with those  
 625 derived from experimental 2D SEM data, have been computed via kernel density estimation,  
 626 see Figure 8.

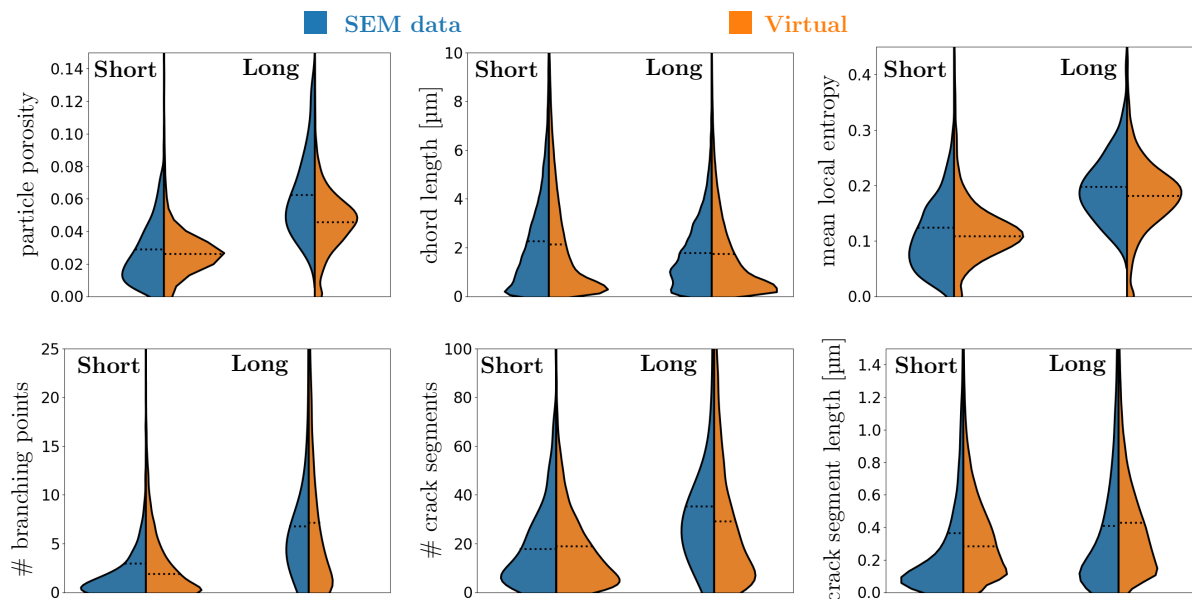


FIGURE 8. Probability densities of porosity, chord lengths, mean local entropy (top row), number of branching points, number and length of crack segments (bottom row). Blue areas indicate densities computed from SEM data, whereas orange areas correspond to densities for planar cross sections of 3D realizations of the extended crack network model. Within each subplot, the left column corresponds to the data set  $\mathcal{G}_{\text{short}}$ , and the right column to  $\mathcal{G}_{\text{long}}$ . The horizontal dashed lines indicate the mean values of the respective descriptors.

627 When comparing the probability densities shown in Figure 8, derived for each case from simu-  
 628 lated and experimental data, respectively, it becomes clearly visible that these pairs of densities  
 629 exhibit similar shapes, indicating a suitable choice of model type and a quite good fit of model  
 630 parameters, for both data sets  $\mathcal{G}_{\text{short}}$  and  $\mathcal{G}_{\text{long}}$ . Even in cases where these pairs of probability  
 631 densities are slightly different from each other, like the densities of the porosity of short-cracked  
 632 particles (top row, left part, left pair of densities), their mean values, represented by horizontal  
 633 dashed lines, fit very well. On the other hand, for example, the porosity distribution of long-  
 634 cracked particles (top row, left part, right pair of densities) exhibits a slightly larger deviation  
 635 of its mean value with respect to the corresponding mean value derived from simulated data.  
 636 Nevertheless, qualitatively, the overall shapes of the probability densities match quite well in  
 637 all cases.

638 In summary, the probability densities derived from simulated and experimentally measured  
 639 image data show a high degree of agreement, indicating that the crack networks observed in 2D  
 640 SEM data are accurately represented by the stochastic 3D model introduced in Section 3.

641 **5.3. Transport-relevant particle descriptors in 3D.** In this section, two geometric particle  
 642 descriptors are considered, which influence the performance of Li-ion batteries, but can only be  
 643 determined adequately if 3D image data is available. However, in general, the acquisition of 3D  
 644 data by tomographic imaging is expensive in terms of time and costs. Therefore, in the present  
 645 paper, these descriptors are estimated by means of a stochastic 3D model, i.e., from realizations  
 646 of the extended crack network model  $P_\theta$ , which has been introduced in Section 3 and calibrated  
 647 by means of 2D image data in Section 4.

648 Thus, in the following, we consider a cracked particle  $P = (\Xi_{\text{solid}}, \Xi_{\text{crack}})$ , where  $\Xi_{\text{solid}}, \Xi_{\text{crack}} \subset$   
 649  $\mathbb{R}^3$ , drawn from the extended crack network model  $P_\theta$ , and we consider its pristine counterpart  
 650  $P_{\text{pr}} = (\Xi_{\text{solid}}^{(\text{pr})}, \emptyset)$  with  $\Xi_{\text{solid}}^{(\text{pr})} = \Xi_{\text{solid}} \cup \Xi_{\text{crack}} \subset \mathbb{R}^3$ , which serves as input for  $P_\theta$ . Furthermore,  
 651 by  $\Xi_{\text{BG}} = \mathbb{R}^3 \setminus \Xi_{\text{solid}}^{(\text{pr})}$  we denote the background of both particles,  $P_{\text{pr}}$  and  $P$ .

652 In particular, relative shortest path lengths from active material of  $P$  to electrolyte (located  
 653 in cracks and/or background) are considered. Note that this is an important particle descriptor,  
 654 since during delithiation, lithium ions migrate from the active material to the surface of the  
 655 particle, where deintercalation occurs. Moreover, we investigate the specific surface area of  
 656 particles, showing how it is affected by cracking. Clearly, this is also a transport-relevant  
 657 particle descriptor, because it characterizes the intercalating surface of a particle.

658 **Relative shortest path lengths.** The paths from randomly chosen locations within the active  
 659 material to electrolyte are analyzed to investigate the transport of Li during delithiation. First,  
 660 the case is considered that particles are embedded in liquid electrolyte, where open porosity  
 661 cracks are filled with electrolyte and transport path lengths may decrease. Furthermore, to  
 662 demonstrate that the extended crack network model  $P_\theta$  introduced in Section 3 is not limited  
 663 to Li-ion batteries with liquid electrolyte, the case of solid electrolyte is considered to mimic  
 664 the behavior of all-solid-state batteries. Then, contrary to batteries with liquid electrolyte,  
 665 cracks caused by cycling are not penetrated with electrolyte. Thus, cracks can be considered as  
 666 obstacles to ion transport, which may increase transport path lengths.

667 A powerful tool to analyze transport paths within a given phase of a two-phase material is the  
 668 so-called geodesic tortuosity. It is a purely geometric descriptor, see e.g. [75], which is usually  
 669 estimated on image data by considering two parallel planes in  $\mathbb{R}^3$ , the starting plane and the  
 670 target plane, denoted by  $E_S$  and  $E_T$  in the following. Then, for each  $x \in E_S$ , the length of the  
 671 shortest path to the target plane  $E_T$  within the transport phase is determined and normalized  
 672 by the distance between the planes  $E_S$  and  $E_T$ . For estimating the geodesic tortuosity in the  
 673 formal framework of random closed sets, we refer to [76]. In the present paper, the concept of  
 674 geodesic tortuosity is generalized by considering arbitrary starting and target sets  $H_S, H_T \subset \mathbb{R}^3$   
 675 such that  $H_S \cap H_T = \emptyset$ .

676 To investigate delithiation in the case of liquid electrolyte (LE), the shortest paths from  
 677 active material to electrolyte are determined by means of simulated 3D image data. For this,  
 678 the starting and target sets  $H_S, H_T$  are discretized, where  $H_S = \Xi_{\text{solid}}$  and  $H_T = \Xi_{\text{crack}} \cup \Xi_{\text{BG}}$ .  
 679 Note that the union  $\Xi_{\text{crack}} \cup \Xi_{\text{BG}}$  of cracks and background forms the continuous representation  
 680 of the target set, since cracks are filled with liquid electrolyte. On the other hand, to mimic  
 681 the behavior of so-called all-solid-state batteries with solid electrolyte (SE), where cracks serve  
 682 as obstacle, the starting and target sets are given by  $H_S = \Xi_{\text{solid}}$  and  $H_T = \Xi_{\text{BG}}$ . In Figure 9,  
 683 examples of shortest paths are shown for the cases of liquid and solid electrolyte, alongside with  
 684 shortest paths in the corresponding pristine (i.e. non-cracked) particle.

685 For each  $x \in H_S$ , the length of the shortest path within the active material from  $x \in H_S$  to  
 686 the target set  $H_T$  is determined, where the transport phase is given by the set  $\Xi = \Xi_{\text{solid}}$  for  
 687 a cracked particle, and by  $\Xi = \Xi_{\text{solid}}^{(\text{pr})} = \Xi_{\text{solid}} \cup \Xi_{\text{crack}}$  for the corresponding pristine particle.  
 688 To compute these shortest path lengths, denoted by  $\gamma_\Xi(x, H_T)$ , Dijkstra's algorithm [77] was  
 689 utilized, as implemented in the python package `dijkstra3D`.

690 Moreover, to investigate how cracking affects the shortest path lengths, we consider relative  
 691 shortest path lengths, denoted by  $\tau_{\text{LE}}(x, P)$  for liquid electrolyte and by  $\tau_{\text{SE}}(x, P)$  for solid  
 692 electrolyte. These quantities are determined by normalizing the shortest path length  $\gamma_\Xi(x, H_T)$ ,  
 693 from  $x \in H_S$  to the target set  $H_T$  within the transport phase  $\Xi = \Xi_{\text{solid}}$  of a cracked particle, by

694 the length of the corresponding shortest path within the solid phase  $\Xi_{\text{solid}}^{(\text{pr})}$  of the pristine particle  
 695  $P_{\text{pr}}$ . Note that the shortest path within the pristine particle represents the shortest path from  
 696 the  $x \in H_S$  to the electrolyte before the particle is cracked. Thus, formally, the relative shortest  
 697 path lengths  $\tau_{\text{LE}}(x, P)$  and  $\tau_{\text{SE}}(x, P)$  for liquid and solid electrolyte, respectively, are as follows:

$$\tau_{\text{LE}}(x, P) = \frac{\gamma_{\Xi_{\text{solid}}}(x, \Xi_{\text{crack}} \cup \Xi_{\text{BG}})}{\gamma_{\Xi_{\text{solid}}^{(\text{pr})}}(x, \Xi_{\text{BG}})}, \quad \tau_{\text{SE}}(x, P) = \frac{\gamma_{\Xi_{\text{solid}}}(x, \Xi_{\text{BG}})}{\gamma_{\Xi_{\text{solid}}^{(\text{pr})}}(x, \Xi_{\text{BG}})} \quad (18)$$

698 for each  $x \in H_S = \Xi_{\text{solid}}$ , where  $\Xi_{\text{solid}}^{(\text{pr})} = \Xi_{\text{solid}} \cup \Xi_{\text{crack}}$ .

699 From Eq. (18) we get that  $\tau_{\text{LE}}(x, P) \leq 1$  and  $\tau_{\text{SE}}(x, P) \geq 1$  for each  $x \in H_S = \Xi_{\text{solid}}$ . This  
 700 indicates a decrease of shortest path lengths caused by cracking in the case of liquid electrolyte,  
 701 and an increase for solid electrolyte, as expected.

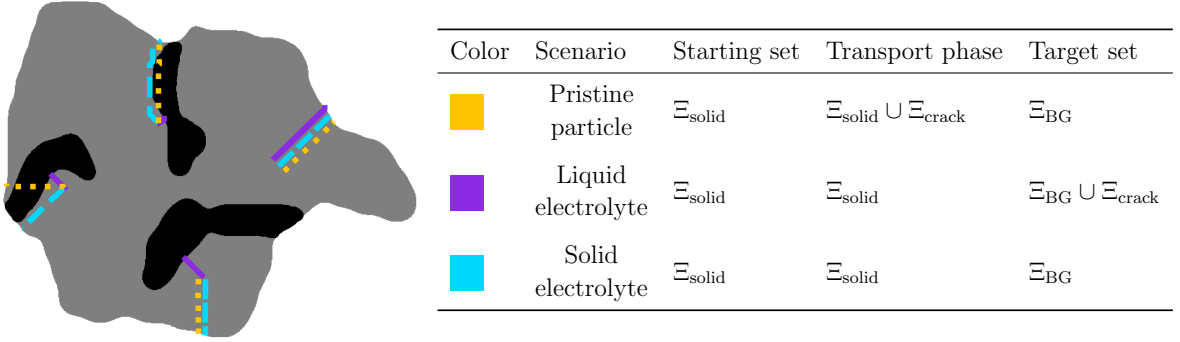


FIGURE 9. Shortest paths from active material (grey) to electrolyte, avoiding cracks (black); for a cracked particle embedded in liquid (purple) and solid (blue) electrolyte, respectively, and for the corresponding pristine particle (orange).

702 Finally, we consider the mean relative shortest path lengths  $\tau_{\text{LE}}(P)$  and  $\tau_{\text{SE}}(P)$ , which are de-  
 703 termined by averaging the relative shortest path lengths  $\tau_{\text{LE}}(x, P)$  and  $\tau_{\text{SE}}(P)$  given in Eq. (18)  
 704 over all  $x \in \Xi_{\text{solid}}$ . The concept of relative shortest path lengths is visualized in Figure 10 for  
 705 both kinds of (liquid and solid) electrolyte.

706 **Relative specific surface area.** Another descriptor related to effective properties of a particle  
 707  $P = (\Xi_{\text{solid}}, \Xi_{\text{crack}})$  is its specific surface area  $\sigma(P)$ . It indicates its surface area per unit volume  
 708 and is formally given by

$$\sigma(P) = \frac{\mathcal{H}_2(\partial\Xi_{\text{solid}})}{\nu_3(\Xi_{\text{solid}})},$$

709 where  $\mathcal{H}_2(\cdot)$  denotes the 2-dimensional Hausdorff measure,  $\nu_3(\cdot)$  the 3-dimensional Lebesgue  
 710 measure and  $\partial\Xi$  the boundary of a set  $\Xi$ . Note that  $\mathcal{H}_2(\cdot)$  measures the area of a 2-dimensional  
 711 manifold and  $\nu_3(\cdot)$  the volume of a 3-dimensional set. Recall that in the present paper model  
 712 realizations are voxelized data. Therefore, the surface area of  $\Xi_{\text{solid}}$  is estimated using the  
 713 algorithm presented in [78] and the volume by counting voxels associated with  $\Xi_{\text{solid}}$ .

714 To investigate the change of the specific surface area caused by cracking, the relative specific  
 715 surface area, given by

$$\sigma_{\text{rel}}(P) = \frac{\sigma(P)}{\sigma(P_{\text{pr}})},$$

716 is considered, where  $P_{\text{pr}}$  denotes the underlying pristine particle corresponding to  $P$ . Note that  
 717 the relative specific surface area  $\sigma_{\text{rel}}(P)$  of  $P$  quantifies the increase of surface area per unit  
 718 volume due to cracking. In particular,  $\sigma_{\text{rel}}(P) = 1$  indicates no change, while larger values of  
 719  $\sigma_{\text{rel}}(P)$  represent an increase in specific surface area caused by cracking. For example,  $\sigma_{\text{rel}}(P) =$   
 720  $2$  indicates a doubling of the specific surface area. Notably, in a real Li-ion battery system, the  
 721 increase in specific surface area due to cracking is only beneficial for liquid electrolyte systems.  
 722 Additionally, the relative activity of newly exposed surfaces to electrochemical reactions will  
 723 depend on the availability of an electron at the surface between the electrolyte and active  
 724 material phase, which is not considered in the present work.

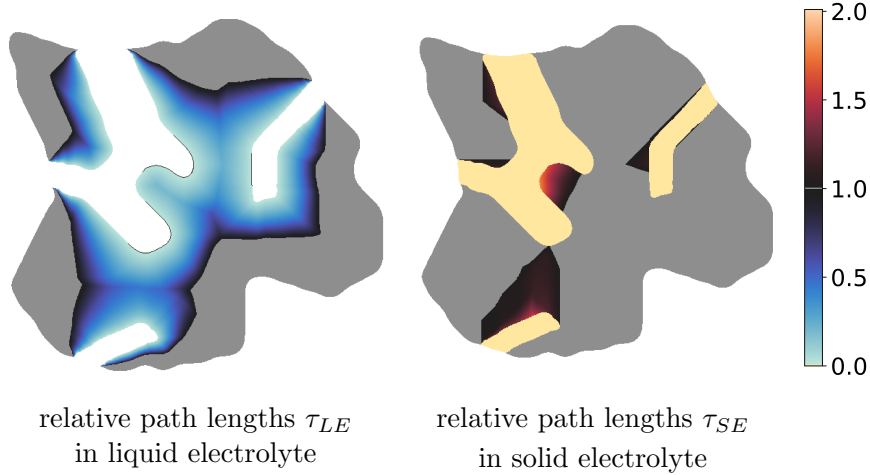


FIGURE 10. Relative shortest path lengths  $\tau_{\text{LE}}(x, P)$  and  $\tau_{\text{SE}}(x, P)$  for liquid (left) and solid electrolyte (right). Note that white indicates electrolyte, while bright yellow (right) indicate obstacles, formed by cracks. Additionally, gray within the particles corresponds to relative path lengths equal to one, indicating no change in the shortest path length due to cracking.

725 **5.4. Structural analysis of simulated 3D particles.** We now deploy the stochastic 3D  
 726 model  $P_{\hat{\theta}}$  of cracked particles that has been calibrated by means of 2D data to investigate the  
 727 transport-relevant descriptors stated in Section 5.3 for simulated 3D particles drawn from  $P_{\hat{\theta}}$ .  
 728 In particular, we investigate the probability distributions of the (relative) specific surface area  
 729 and the mean relative shortest path length (for solid and liquid electrolyte) associated with  
 730 the stochastic 3D model  $P_{\hat{\theta}}$ . More precisely, we will provide a detailed discussion of the cor-  
 731 responding probability densities of these descriptors, separately for the stochastic 3D model  
 732  $P_{\hat{\theta}_{\text{short}}}$  calibrated to the data set  $\mathcal{G}_{\text{short}}$ , and for  $P_{\hat{\theta}_{\text{long}}}$  calibrated to  $\mathcal{G}_{\text{long}}$ .

733 First, we draw 200 realizations from  $P_{\hat{\theta}_{\text{short}}}$  which we denote by  $P^{(i)}$  for  $i = 1, \dots, 200$ . By  
 734 computing the transport-relevant descriptors introduced in Section 5.3 for these realizations,  
 735 we obtain four sample data sets, denoted by  $\{\tau_{\text{LE}}(P^{(i)})\}_{i=1}^{200}$ ,  $\{\tau_{\text{SE}}(P^{(i)})\}_{i=1}^{200}$ ,  $\{\sigma(P^{(i)})\}_{i=1}^{200}$  and  
 736  $\{\sigma_{\text{rel}}(P^{(i)})\}_{i=1}^{200}$ . Then, by means of kernel density estimation on each of these four sets, we get  
 737 probability densities of the corresponding transport-relevant particle descriptors, see the blue  
 738 plots in Figures 11 and 12. Furthermore, the same procedure was applied to 200 realizations  
 739 drawn from  $P_{\hat{\theta}_{\text{long}}}$  to determine probability densities of the particle descriptors introduced in  
 740 Section 5.3, see the green plots in Figures 11 and 12.

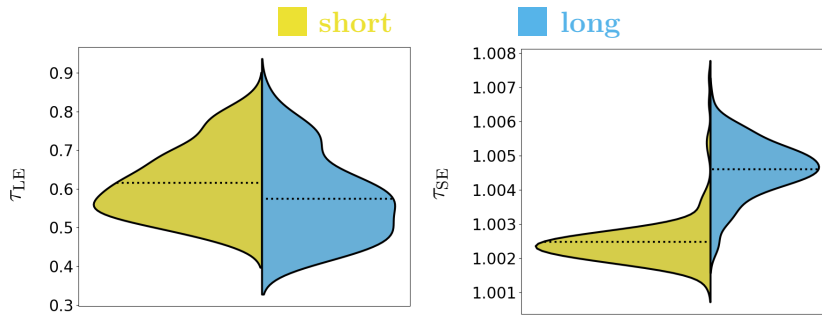


FIGURE 11. Probability densities of mean relative shortest path lengths  $\tau_{LE}(P)$  and  $\tau_{SE}(P)$  for liquid (left) and solid electrolyte (right). Each subfigure shows two probability densities, where the green (left) areas correspond to the probability densities computed from short-cracked particles and the blue (right) areas indicate the probability densities derived from long-cracked particles.

741 Note that the transport-relevant particle descriptors introduced in Section 5.3, with the  
 742 exception of the specific surface area  $\sigma(P)$ , are computed by comparing descriptors of simulated  
 743 cracked particles with those of the underlying pristine counterparts. Consequently, for pristine  
 744 particles the mean relative shortest path length as well as the relative specific surface area  
 745 are deterministic (i.e. non-random) quantities, being equal to 1. Therefore, when considering  
 746 probability distributions of relative transport-relevant descriptors, only the specific surface area  
 747 of pristine particles, see Figure 12 (left, purple), is of further interest.

748 The comparison of the probability densities shown in Figures 11 and 12 provides us with  
 749 quantitative insight into the transport behavior of cracked 3D particles, even though initially  
 750 only 2D data was available. For example, an intuitive result is that shortest path lengths  
 751 decrease after cracking for liquid electrolyte systems, i.e., the mean relative shortest path lengths  
 752 are typically smaller than 1, see Figure 11 (left). This is to be expected as cracks can be flooded  
 753 by the liquid electrolyte leading to shorter transport paths. On the other hand, shortest path  
 754 lengths increase for solid electrolyte, even though the relative increase is marginal, i.e., only  
 755 slightly above 1, see Figure 11 (right).

756 These general trends can be observed for both variants of the calibrated stochastic 3D model,  
 757  $P_{\hat{\theta}_{\text{short}}}$  and  $P_{\hat{\theta}_{\text{long}}}$ . However, when comparing both models, we observe that—in the case of liquid  
 758 electrolyte—mean shortest path lengths seem to decrease more significantly for long-cracked  
 759 particles rather than for short-cracked ones. For solid electrolyte systems, the difference in  
 760 mean shortest path lengths between short- and long-cracked particles is much smaller, taking  
 761 into account the finer length scale of the y-axis on the right-hand side of Figure 11.

762 In the case of liquid electrolyte, an explanation for the existence of shorter transport paths  
 763 is the fact that transport paths, which are originating in the active material phase, have the  
 764 option to end at the interface between active material and crack phases, instead of ending at  
 765 the background. In other words, caused by cracking, the set of possible endpoints of transport  
 766 paths originating in the active material becomes larger which possibly leads to a decrease of  
 767 shortest path lengths. On the other hand, in the case of solid electrolyte, only a small fraction  
 768 of shortest transport paths seems to be affected by cracking (which can cause obstacles to form).  
 769 Consequently, we observe mean relative shortest path lengths close to 1, see Figure 11 (right).  
 770 From the 2D illustrations of relative shortest path lengths in liquid and solid electrolyte, shown  
 771 in Figure 10, a visual impression of this effect can be obtained.

772 With respect to specific surface area, see Figure 12 (left), we observe that both scenarios (i.e.,  
 773 short- and long-cracked particles) lead to an increase of this geometric particle descriptor—  
 774 an effect that is more pronounced for long-cracked particles generated by  $P_{\hat{\theta}_{\text{long}}}$ . Moreover,  
 775 the relative specific surface area quantifies this increase compared to the underlying pristine  
 776 particle. Short-cracked particles exhibit an average increase in their specific surface area by a  
 777 factor of 1.5 in comparison to their pristine counterparts, whereas this factor is equal to 2 for  
 778 long-cracked particles, see Figure 12 (right).

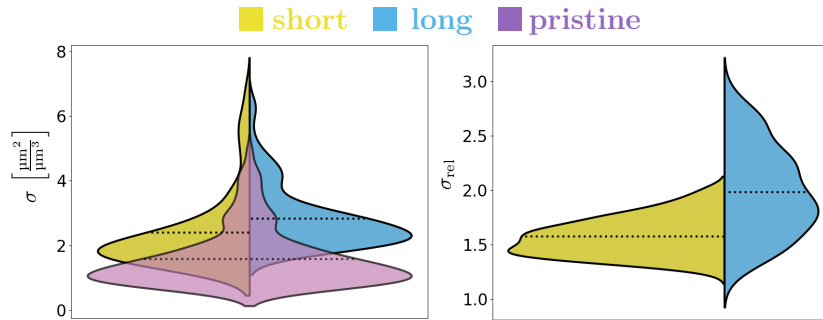


FIGURE 12. Left: Probability densities of the specific surface area  $\sigma(P)$  for pristine particles (purple) and for cracked particles drawn from the stochastic 3D models  $P_{\hat{\theta}_{\text{short}}}$  (green) and  $P_{\hat{\theta}_{\text{long}}}$  (blue). Right: Probability densities of the relative specific surface area  $\sigma_{\text{rel}}(P)$  for cracked particles drawn from  $P_{\hat{\theta}_{\text{short}}}$  (green) and  $P_{\hat{\theta}_{\text{long}}}$  (blue), respectively.

779 In summary, it is important to note that the transport-relevant particle descriptors discussed  
 780 in this section, namely the mean relative shortest path length and the relative specific surface  
 781 area of cracked particles, are just examples of numerous further descriptors of 3D particles, which  
 782 cannot be adequately determined from 2D cross sections. Thus, the stereological approach to  
 783 stochastic 3D modeling of cracked particles proposed in the present paper can be used in future  
 784 research to provide geometry input for spatially resolved numerical modeling and simulation,  
 785 with the goal to derive quantitative structure-property relationships of cathode materials in  
 786 Li-ion batteries, e.g. with respect to mechanical and electrochemical properties.

787

## 6. CONCLUSION

788 This paper presents a novel approach for generating virtual 3D cathode particles with crack  
 789 networks that are statistically equivalent to those observed in 2D cross-sections of experimentally  
 790 manufactured particles, where a stochastic 3D model is developed which inserts cracks into  
 791 virtually generated NMC particles, requiring solely 2D image data for model calibration.

792 An essential advantage of our model is that it enables the generation and analysis of a large  
 793 number of virtual particle morphologies in 3D, whose planar 2D sections exhibit similar statistics  
 794 as planar sections of experimentally manufactured particles. This computer-based procedure  
 795 is cheaper, faster and more reliable than analyzing just a few experimentally manufactured  
 796 particles. One reason for this is the circumstance that the acquisition of tomographic image  
 797 data for a statistically representative number of particles can be expensive in both time and  
 798 resources.

799 On the other hand, virtual particles generated by our stochastic 3D model allow for a more  
 800 rigorous quantification of cracked NMC particles, i.e., by characterizing their 3D morphology

801 and, subsequently, by conducting spatially resolved mechanical and electrochemical simulations  
802 examining their structure-properties relationships. This supports the analysis and comparison  
803 of different cycling conditions such as varying C-rate, operating temperature, or number of  
804 cycles.

805 It is important to emphasize that the stochastic model presented in this paper for the 3D  
806 morphology of cracked NMC particles is characterized by a small number of (nine) interpretable  
807 parameters. In contrast to convolutional neural networks (CNNs), which have tens of thousands  
808 to several million trainable parameters, our stochastic 3D model has no “black-box” behavior  
809 and represents a low-parametric, transparent alternative to CNNs.

810 Moreover, our stochastic 3D model can be modified to involve further features that might in-  
811 fluence cracking, e.g., by generating cracks in dependence of the crystallographic orientation of  
812 adjacent intraparticulate grains. For example, this can be achieved by considering the misorien-  
813 tation between two neighboring grains, either replacing or supplementing the spatial alignment  
814 of the joint grain boundary. To implement such a modified model, orientation data of NMC  
815 particles is required, which could be derived, e.g., from EBSD measurements. Further, the  
816 presented stochastic 3D crack model could be generalized by allowing for inhomogeneous and  
817 anisotropic crack networks, e.g., by conditioning the cracking probabilities on radial distances  
818 to the particle center or on the transport direction within the electrode.

819 Another advantage of our stereological modeling approach is the fact that it allows for the  
820 estimation of chemo-mechanical properties from 2D images. More precisely, since our model  
821 only requires 2D images to generate realistic 3D particle morphologies, it is possible to use  
822 these 3D morphologies as geometry input for spatially resolved simulations of effective particle  
823 properties, which would be otherwise impossible to get them on the basis of 2D image data.

824

## ACKNOWLEDGEMENT

825 This work was authored in-part by Alliance for Sustainable Energy, LLC, the manager and  
826 operator of the National Renewable Energy Laboratory for the U.S. Department of Energy  
827 (DOE) under Contract No. DE-AC36-08GO28308. Funding was provided by DOE’s Vehicle  
828 Technologies Office, Extreme Fast Charge and Cell Evaluation of Lithium-ion Batteries Pro-  
829 gram, Jake Herb, Technology Manager. The views expressed in the article do not necessarily  
830 represent the views of the DOE or the U.S. Government.

831

## REFERENCES

- 832 [1] E. J. Cairns and P. Albertus. Batteries for electric and hybrid-electric vehicles. *Annu. Rev.*  
833 *Chem. Biomol. Eng.*, 1:299–320, 2010.
- 834 [2] M. Tariq, A. I. Maswood, C. J. Gajanayake, and A. Gupta. Aircraft batteries: Current  
835 trend towards more electric aircraft. *IET Electr. Syst. Transp.*, 7:93–103, 2016.
- 836 [3] J. E. Harlow, X. Ma, J. Li, E. Logan, Y. Liu, N. Zhang, L. Ma, S. L. Glazier, M. M. E.  
837 Cormier, M. Genovese, S. Buteau, A. Cameron, J. E. Stark, and J. R. Dahn. A wide range  
838 of testing results on an excellent lithium-ion cell chemistry to be used as benchmarks for  
839 new battery technologies. *J. Electrochem. Soc.*, 166:A3031, 2019.
- 840 [4] A. M. Colclasure, A. R. Dunlop, S. E. Trask, B. J. Polzin, A. N. Jansen, and K. Smith.  
841 Requirements for enabling extreme fast charging of high energy density Li-ion cells while  
842 avoiding lithium plating. *J. Electrochem. Soc.*, 166:A1412–A1424, 2019.

- 843 [5] Z. Li, N. A. Chernova, M. Roppolo, S. Upreti, C. Petersburg, F. M. Alamgir, and M. S.  
844 Whittingham. Comparative study of the capacity and rate capability of  $\text{LiNi}_y\text{Mn}_y\text{Co}_{1-2y}\text{O}_2$   
845 ( $y = 0.5, 0.45, 0.4, 0.33$ ). *J. Electrochem. Soc.*, 158, 2011.
- 846 [6] A. Manthiram, B. Song, and W. Li. A perspective on nickel-rich layered oxide cathodes  
847 for lithium-ion batteries. *Energy Storage Mater.*, 6:125–139, 2017.
- 848 [7] J. Kim, H. Lee, H. Cha, M. Yoon, M. Park, and J. Cho. Prospect and reality of Ni-rich  
849 cathode for commercialization. *Adv. Energy Mat.*, 8:1702028, 2018.
- 850 [8] J. Li, H. Liu, J. Xia, A. R. Cameron, M. Nie, G. A. Botton, and J. Dahn. The impact of  
851 electrolyte additives and upper cut-off voltage on the formation of a rocksalt surface layer  
852 in  $\text{LiNi}_{0.8}\text{Mn}_{0.1}\text{Co}_{0.1}\text{O}_2$  electrodes. *J. Electrochem. Soc.*, 164:A655–A665, 2017.
- 853 [9] T. Li, X.-Z. Yuan, L. Zhang, D. Song, K. Shi, and C. Bock. Degradation mechanisms and  
854 mitigation strategies of nickel-rich NMC-based lithium-ion batteries. *Electrochem. Energy*  
855 *Rev.*, 3:43–80, 2019.
- 856 [10] S.-L. Cui, X. Zhang, X.-W. Wu, S. Liu, Z. Zhou, G.-R. Li, and X.-P. Gao. Understanding  
857 the structure–performance relationship of lithium-rich cathode materials from an oxygen-  
858 vacancy perspective. *ACS Appl. Mater. Interfaces.*, 12(42):47655–47666, 2020.
- 859 [11] T. R. Tanim, Z. Yang, A. M. Colclasure, P. R. Chinnam, P. Gasper, S.-B. Son, P. J.  
860 Weddle, E. J. Dufek, I. Bloom, K. Smith, C. C. Dickerson, M. C. Evans, A. R. Dunlop,  
861 S. E. Trask, B. J. Polzin, and A. N. Jansen. Extended cycle life implications of fast charging  
862 for lithium-ion battery cathode. *Energy Storage Mater.*, 41:656–666, 2021.
- 863 [12] T. R. Tanim, P. J. Weddle, Z. Yang, A. M. Colclasure, H. Charalambous, D. P. Finegan,  
864 Y. Lu, M. Preefer, S. Kim, J. Allen, F. L. E. Usseglio-Viretta, P. R. Chinnam, I. Bloom,  
865 E. J. Dufek, K. Smith, G. Chen, K. M. Wiaderek, J. W. Nelson, and Y. Ren. Enabling  
866 extreme fast-charging: Challenges at the cathode and mitigation strategies. *Adv. Energy*  
867 *Mater.*, 12:2202795, 2022.
- 868 [13] E. J. Dufek, D. P. Abraham, I. Bloom, B.-R. Chen, P. R. Chinnam, A. M. Colclasure,  
869 K. L. Gering, M. K. S. Kim, W. Mai, D. C. Robertson, M.-T. F. Rodrigues, K. Smith,  
870 T. R. Tanim, F. L. E. Usseglio-Viretta, and P. J. Weddle. Developing extreme fast charge  
871 battery protocols – A review spanning materials to systems. *J. Power Sources*, 526:231129,  
872 2022.
- 873 [14] J. Liu, Z. Bao, Y. Cui, E. J. Dufek, J. B. Goodenough, P. Khalifah, Q. Li, B. Liaw,  
874 P. Liu, A. Manthiram, Y. S. Meng, V. R. Subramanian, M. F. Toney, V. V. Viswanathan,  
875 M. S. Whittingham, J. Xiao, W. Xu, J. Yang, X.-Q. Yang, and J.-G. Zhang. Pathways for  
876 practical high-energy long-cycling lithium metal batteries. *Nat. Energy*, 4:180–186, 2019.
- 877 [15] Y. Wang, W. Zhang, L. Chen, S. Shi, and J. Liu. Quantitative description on struc-  
878 ture–property relationships of Li-ion battery materials for high-throughput computations.  
879 *Sci. Technol. Adv. Mater.*, 18(1):134–146, 2017.
- 880 [16] C. Wang, R. Yu, S. Hwang, J. Liang, X. Li, C. Zhao, Y. Sun, J. Wang, N. Holmes, R. Li,  
881 H. Huang, S. Zhao, L. Zhang, S. Lu, D. Su, and X. Sun. Single crystal cathode enabling  
882 high-performance all-solid state lithium-ion batteries. *Energy Storage Mater.*, 30:98–103,  
883 2020.
- 884 [17] K. Taghikhani, P. J. Weddle, R. M. Hoffman, J. R. Berger, and R. J. Kee. Electro-  
885 chemo-mechanical finite-element model of single-crystal and polycrystalline NMC cathode  
886 particles embedded in an argyrodite solid electrolyte. *Electrochim. Acta*, 460:142585, 2023.
- 887 [18] G. Conforto, R. Ruess, D. Schröder, E. Trevisanello, R. Fantin, F. Richter, and J. Janek.  
888 Editors’ choice – Quantification of the impact of chemo-mechanical degradation on the

- 889 performance and cycling stability of NCM-based cathodes in solid-state Li-ion batteries. *J.*  
890 *Electrochem. Soc.*, 168:070546, 2021.
- 891 [19] R. Koerver, I. Aygün, T. Leichtweiß, C. Dietrich, W. Zhang, J. O. Binder, P. Hartmann,  
892 W. G. Zeier, and J. Janek. Capacity fade in solid-state batteries: Interphase formation and  
893 chemomechanical processes in nickel-rich layered oxide cathodes and lithium thiophosphate  
894 solid electrolytes. *Chem. Mater.*, 29:5574–5582, 2017.
- 895 [20] Y. Yang, R. Xu, K. Zhang, S.-J. Lee, L. Mu, P. Liu, C. Waters, S. Spence, Z. Xu, C. Wei,  
896 D. Kautz, Q. Yuan, Y. Dong, Y.-S. Yu, X. Xiao, H.-K. Lee, P. Pianetta, P. Cloetens, J.-S.  
897 Lee, K. Zhao, F. Lin, and Y. Liu. Quantification of heterogeneous degradation in Li-ion  
898 batteries. *Adv. Energy Mater.*, 9:1900674, 2019.
- 899 [21] W. Li. Review – An unpredictable hazard in lithium-ion batteries from transition metal  
900 ions: Dissolution from cathodes, deposition on anodes and elimination strategies. *J. Elec-*  
901 *trochem. Soc.*, 167:090514, 2020.
- 902 [22] R. Jung, M. Metzger, F. Maglia, C. Stinner, and H. A. Gasteiger. Oxygen release and  
903 its effect on the cycling stability of  $\text{LiNi}_x\text{Mn}_y\text{Co}_z\text{O}_2$  (NMC) cathode materials for Li-ion  
904 batteries. *J. Electrochem. Soc.*, 164:A1361–A1377, 2017.
- 905 [23] R. Jung, P. Strobl, F. Maglia, C. Stinner, and H. A. Gasteiger. Temperature dependence of  
906 oxygen release from  $\text{LiNi}_{0.6}\text{Mn}_{0.2}\text{Co}_{0.2}\text{O}_2$  (NMC622) cathode materials for Li-ion batteries.  
907 *J. Electrochem. Soc.*, 165:A2869, 2018.
- 908 [24] R. Xu, L. S. de Vasconcelos, and K. Zhao. Mechanical and structural degradation of  
909  $\text{LiNi}_x\text{Mn}_y\text{Co}_z\text{O}_2$  cathode in Li-ion batteries: An experimental study. *J. Electrochem. Soc.*,  
910 164:A333–A3341, 2017.
- 911 [25] R. Xu and K. Zhao. Corrosive fracture of electrodes in Li-ion batteries. *J. Mech. Phys.*  
912 *Solids*, 121:258–280, 2018.
- 913 [26] J. Vetter, P. Novák, M. R. Wagner, C. Veit, K.-C. Möller, J. O. Besenhard, M. Winter,  
914 M. Wohlfahrt-Mehrens, C. Vogler, and A. Hammouche. Aging mechanisms in lithium-ion  
915 batteries. *J. Power Sources*, 147:269–281, 2005.
- 916 [27] S. Lee, L. Su, A. Mesnier, Z. Cui, and A. Manthiram. Cracking vs. surface reactivity in  
917 high-nickel cathodes for lithium-ion batteries. *Joule*, 7:2430–2444, 2023.
- 918 [28] T. R. Tanim, Z. Yang, D. P. Finegan, P. R. Chinnam, Y. Lin, P. J. Weddle, I. Bloom,  
919 A. M. Colclasure, E. J. Dufek, J. Wen, Y. Tsai, M. Evans, K. Smith, J. M. Allen, C. C.  
920 Dickerson, A. H. Quinn, A. R. Dunlop, S. E. Trask, and A. N. Jansen. A comprehensive  
921 understanding of the aging effects of extreme fast charging on high Ni NMC cathode. *Adv.*  
922 *Energy Mater.*, 12:2103712, 2022.
- 923 [29] H. H. Ryu, K. J. Park, C. S. Yoon, and Y. K. Sun. Capacity fading of Ni-rich  
924  $\text{Li}[\text{Ni}_x\text{Co}_y\text{Mn}_{1-x-y}]\text{O}_2$  ( $0.6 \leq x \leq 0.95$ ) cathodes for high-energy-density lithium-ion bat-  
925 teries: Bulk or surface degradation? *Chem. Mater.*, 30:1155–1163, 2018.
- 926 [30] D. Meng, Z. Xue, G. Chen, D. Zhou, Y.-S. He, Z.-F. Ma, Y. Liu, and L. Li. Multiscale  
927 correlative imaging reveals sequential and heterogeneous degradations in fast-charging bat-  
928 teries. *Energy Environ. Sci.*, 17:4658, 2024.
- 929 [31] J. Xu, B. Paredes-Goyes, Z. Su, M. Scheel, T. Weitkamp, A. Demorttère, and A. A. Franco.  
930 Computational model for predicting particle fracture during electrode calendaring. *Batter-*  
931 *ies & Supercaps*, 6:e202300371, 2023.
- 932 [32] H. Bockholt, M. Indrikova, A. Netz, F. Golks, and A. Kwade. The interaction of consecutive  
933 process steps in manufacturing of lithium-ion battery electrodes with regard to structural  
934 electrochemical properties. *J. Power Sources*, 325:140–151, 2016.

- 935 [33] J. M. Allen, P. J. Weddle, A. Verma, A. Mallarapu, F. Usseglio-Viretta, D. P. Finegan,  
936 A. M. Colclasure, W. Mai, V. Schmidt, O. Furat, D. Diercks, T. Tanim, and K. Smith.  
937 Quantifying the influence of charge rate and cathode-particle architectures on degradation  
938 of Li-ion cells through 3D continuum-level damage models. *J. Power Sources*, 512:230415,  
939 2021.
- 940 [34] J. Kim, H. Lee, H. Cha, M. Yoon, M. Park, and H. Cho. Prospect and reality of Ni-rich  
941 cathode for commercialization. *Adv. Energy Mater.*, 8:1702028, 2018.
- 942 [35] K. Taghikhani, P. J. Weddle, J. R. Berger, and R. J. Kee. Modeling coupled chemo-  
943 mechanical behavior of randomly oriented NMC811 polycrystalline Li-ion battery cathodes.  
944 *J. Electrochem. Soc.*, 168:080511, 2021.
- 945 [36] Y. Bai, K. Zhao, Y. Liu, P. Stein, and B.-X. Xu. A chemo-mechanical grain boundary model  
946 and its application to understand the damage of Li-ion battery materials. *Scr. Mater.*, 183:  
947 45–49, 2020.
- 948 [37] A. Singh, J. Song, W. Li, T. Martin, H. Xu, D. P. Finegan, and J. Zhu. Microstructure-  
949 chemomechanics relations of polycrystalline cathodes in solid-state batteries. *Extreme*  
950 *Mech. Lett.*, 69:102164, 2024.
- 951 [38] W.-X. Chen, J. M. Allen, S. Rezaei, O. Furat, V. Schmidt, A. Singh, P. J. Weddle, K. Smith,  
952 and B.-X. Xu. Cohesive phase-field chemo-mechanical simulations of inter- and trans-  
953 granular fractures in polycrystalline NMC cathode via image-based 3D reconstruction. *J.*  
954 *Power Sources*, 596:234054, 2024.
- 955 [39] W. M. Dose, C. Xu, C. P. Grey, and M. F. L. D. Volder. Effect of anode slippage on  
956 cathode cutoff potential and degradation mechanisms in Ni-rich Li-ion batteries. *Cell Rep.*  
957 *Phys. Sci.*, 1:100253, 2020.
- 958 [40] O. Furat, D. P. Finegan, Z. Yang, T. R. Tanim, K. Smith, and V. Schmidt. Quantifying  
959 the impact of charge rate and number of cycles on structural degeneration of Li-ion battery  
960 electrodes. *J. Electrochem. Soc.*, 169:100541, 2022.
- 961 [41] O. Furat, D. P. Finegan, Z. Yang, M. Neumann, S. Kim, T. R. Tanim, P. Weddle, K. Smith,  
962 and V. Schmidt. Quantifying the impact of operating temperature on cracking in battery  
963 electrodes, using super-resolution of microscopy images and stereology. *Energy Storage*  
964 *Mater.*, 64:103036, 2024.
- 965 [42] S. H. Jung, U.-H. Kim, J.-H. Kim, S. Jun, C. Yoon, S. Jung, and Y.-K. Sun. Ni-rich  
966 layered cathode materials with electrochemo-mechanically compliant microstructures for  
967 all-solid-state Li batteries. *Adv. Energy Mater.*, 10:1903360, 2020.
- 968 [43] S.-K. Jung, H. Gwon, J. Hong, K.-Y. Park, D.-H. Seo, H. Kim, J. Hyun, W. Yang, and  
969 K. Kang. Understanding the degradation mechanisms of  $\text{LiNi}_{0.5}\text{Co}_{0.2}\text{Mn}_{0.3}\text{O}_2$  cathode  
970 material in lithium ion batteries. *Adv. Energy Mater.*, 4:1300787, 2013.
- 971 [44] L. Petrich, D. Westhoff, J. Feinauer, D. P. Finegan, S. R. Daemi, P. R. Shearing, and  
972 V. Schmidt. Crack detection in lithium-ion cells using machine learning. *Comput. Mater.*  
973 *Sci.*, 136:297–305, 2017.
- 974 [45] D. Westhoff, D. P. Finegan, P. R. Shearing, and V. Schmidt. Algorithmic structural seg-  
975 mentation of defective particle systems: A lithium-ion battery study. *J. Microsc.*, 270:  
976 71–82, 2018.
- 977 [46] T. Wilhelm, T. T. V $\ddot{o}$ , O. Furat, U. A. Peuker, and V. Schmidt. Virtual reassembling  
978 of 3D fragments for the data-driven analysis of fracture mechanisms in multi-component  
979 materials. *Comput. Mater. Sci.*, 242:113065, 2024.

- 980 [47] S. Xia, L. Mu, Z. Xu, J. Wang, C. Wei, L. Liu, P. Pianetta, K. Zhao, X. Yu, F. Lin, and  
981 Y. Liu. Chemomechanical interplay of layered cathode materials undergoing fast charging  
982 in lithium batteries. *Nano Energy*, 53:753–762, 2018.
- 983 [48] A. Wade, A. V. Llewlyn, T. M. M. Heenan, C. Tan, D. J. L. Brett, R. Jervis, and P. R.  
984 Shearing. First cycle cracking behavior within Ni-rich cathodes during high-voltage charg-  
985 ing. *J. Electrochem. Soc.*, 170:070513, 2023.
- 986 [49] S. Li, Z. Jiang, J. Han, Z. Xu, C. Wang, H. Huang, C. Yu, S.-J. Lee, P. Pianetta, H. Ohldag,  
987 J. Qiu, J.-S. Lee, F. Lin, K. Zhao, and Y. Liu. Mutual modulation between surface chem-  
988 istry and bulk microstructure within secondary particles of nickel-rich layered oxides. *Nat.*  
989 *Commun.*, 11:1–9, 2020.
- 990 [50] O. Furat, L. Petrich, D. P. Finegan, D. Diercks, F. Usseglio-Viretta, K. Smith, and  
991 V. Schmidt. Artificial generation of representative single Li-ion electrode particle archi-  
992 tectures from microscopy data. *npj Comput. Mater.*, 7:105, 12 2021.
- 993 [51] P. Rieder, M. Neumann, L. Monteiro Fernandes, A. Mulard, H. Proudhon, F. Willot, and  
994 V. Schmidt. Stochastic 3D microstructure modeling of twinned polycrystals for investigat-  
995 ing the mechanical behavior of  $\gamma$ -TiAl intermetallics. *Computational Materials Science*,  
996 238:112922, 2024.
- 997 [52] Y. Zhang, M. Yan, Y. Wan, Z. Jiao, Y. Chen, F. Chen, C. Xia, and M. Ni. High-throughput  
998 3D reconstruction of stochastic heterogeneous microstructures in energy storage materials.  
999 *npj Computational Materials*, 5:11, 2019.
- 1000 [53] J. Han, N. Sharma, and K. Zhao. Computational modeling of coupled mechanical damage  
1001 and electrochemistry in ternary oxide composite electrodes. *J. Power Sources*, 595:234034,  
1002 2024.
- 1003 [54] R. B. F. Willot and H. Trumel. Elastostatic field distributions in polycrystals and cracked  
1004 media. *Phil. Mag.*, 100:661–687, 2020.
- 1005 [55] L. Monteiro Fernandes, P. Rieder, M. Neumann, A. Mulard, H. Proudhon, V. Schmidt, and  
1006 F. Willot. *Effect of Crystallographic Twins on the Elastoplastic Response of Polycrystals*,  
1007 pages 89–103. Springer, 2024.
- 1008 [56] B. Priffling, M. Röding, P. Townsend, M. Neumann, and V. Schmidt. Large-scale statistical  
1009 learning for mass transport prediction in porous materials using 90,000 artificially generated  
1010 microstructures. *Front. Mater.*, 8:786502, 2021.
- 1011 [57] M. Neumann, O. Furat, D. Hlushkou, U. Tallarek, L. Holzer, and V. Schmidt. On  
1012 microstructure-property relationships derived by virtual materials testing with an emphasis  
1013 on effective conductivity. In M. Baum, G. Brenner, J. Grabowski, T. Hanschke, S. Hart-  
1014 mann, and A. Schöbel, editors, *Simulation Science: Proceedings of the Clausthal-Göttingen*  
1015 *International Workshop on Simulation Science*, pages 145–158. Springer, 2017.
- 1016 [58] A. Liebscher, D. Jeulin, and C. Lantuéjoul. Stereological reconstruction of polycrystalline  
1017 materials. *J. Microsc.*, 258(3):190–199, 2015.
- 1018 [59] L. Fuchs, O. Furat, D. Finegan, J. Allen, F. Usseglio-Viretta, B. Ozdogru, P. Weddle,  
1019 K. Smith, and V. Schmidt. Generating multi-scale NMC particles with radial grain ar-  
1020 chitectures, using spatial stochastics and gans. *Preprint available at arXiv: 2407.05333*,  
1021 2024.
- 1022 [60] C. Jung and C. Redenbach. Crack modeling via minimum-weight surfaces in 3D Voronoi  
1023 diagrams. *J. Math. Ind.*, 13:10, 2023.

- 1024 [61] A. Quinn, H. Moutinho, F. Usseglio-Viretta, A. Verma, K. Smith, M. Keyser, and D. Finegan. Electron backscatter diffraction for investigating lithium-ion electrode particle architectures. *Cell Rep. Phys. Sci.*, 1:8, 2020.
- 1025
- 1026
- 1027 [62] S. Van der Walt, J. L. Schönberger, J. Nunez-Iglesias, F. Boulogne, J. D. Warner, N. Yager, E. Gouillart, and T. Yu. scikit-image: Image processing in Python. *PeerJ*, 2:e453, 2014.
- 1028
- 1029 [63] O. Furat, D. P. Finegan, Z. Yang, T. Kirstein, K. Smith, and V. Schmidt. Super-resolving microscopy images of Li-ion electrodes for fine-feature quantification using generative adversarial networks. *npj Comput. Mater.*, 8:68, 2022.
- 1030
- 1031
- 1032 [64] F. Pedregosa, G. Varoquaux, A. Gramfort, V. Michel, B. Thirion, O. Grisel, M. Blondel, P. Prettenhofer, R. Weiss, V. Dubourg, J. Vanderplas, A. Passos, D. Cournapeau, M. Brucher, M. Perrot, and Édouard Duchesnay. Scikit-learn: Machine learning in Python. *Journal of Machine Learning Research*, 12(85):2825–2830, 2011.
- 1033
- 1034
- 1035
- 1036 [65] T. Lee, R. Kashyap, and C. Chu. Building skeleton models via 3-D medial surface axis thinning algorithms. *CVGIP: Graph. Mod. Image Process.*, 56:462–478, 1994.
- 1037
- 1038 [66] A. Okabe, B. Boots, K. Sugihara, and S. N. Chiu. *Spatial Tessellations: Concepts and Applications of Voronoi Diagrams*. J. Wiley & Sons, 2nd edition, 2000.
- 1039
- 1040 [67] S. Chiu, D. Stoyan, W. S. Kendall, and J. Mecke. *Stochastic Geometry and its Applications*. J. Wiley & Sons, 3rd edition, 2013.
- 1041
- 1042 [68] J. Mayer, V. Schmidt, and F. Schweiggert. A unified simulation framework for spatial stochastic models. *Simul. Model. Pract. Theory.*, 12(5):307–326, 2004.
- 1043
- 1044 [69] J. A. Nelder and R. Mead. A simplex method for function minimization. *Comput. J.*, 7:308–313, 1965.
- 1045
- 1046 [70] D. P. Kroese, T. Taimre, and Z. I. Botev. *Handbook of Monte Carlo Methods*. J. Wiley & Sons, 2013.
- 1047
- 1048 [71] A. Baddeley and E. Jensen. *Stereology for Statisticians*. Taylor & Francis, 2004.
- 1049 [72] H. G. Merkus. *Particle Size Measurements: Fundamentals, Practice, Quality*. Springer, 2009.
- 1050
- 1051 [73] J. T. Gostick, Z. A. Khan, T. G. Tranter, M. D. Kok, M. Agnaou, M. Sadeghi, and R. Jervis. PoreSpy: A Python toolkit for quantitative analysis of porous media images. *J. Open Source Softw.*, 4:1296, 2019.
- 1052
- 1053
- 1054 [74] N. Fahlgren, M. Feldman, M. A. Gehan, M. S. Wilson, C. Shyu, D. W. Bryant, S. T. Hill, C. J. McEntee, S. N. Warnasooriya, I. Kumar, T. Ficor, S. Turnipseed, K. B. Gilbert, T. P. Brutnell, J. C. Carrington, T. C. Mockler, and I. Baxter. A versatile phenotyping system and analytics platform reveals diverse temporal responses to water availability in setaria. *Mol. Plant*, 8:1520–1535, 2015.
- 1055
- 1056
- 1057
- 1058
- 1059 [75] L. Holzer, P. Marmet, M. Fingerle, A. Wiegmann, M. Neumann, and V. Schmidt. *Tortuosity and Microstructure Effects in Porous Media: Classical Theories, Empirical Data and Modern Methods*. Springer, 2023.
- 1060
- 1061
- 1062 [76] M. Neumann, C. Hirsch, J. Staněk, V. Beneš, and V. Schmidt. Estimation of geodesic tortuosity and constrictivity in stationary random closed sets. *Scand. J. Stat.*, 46:848–884, 2019.
- 1063
- 1064
- 1065 [77] R. Diestel. *Graph Theory*. Springer, 5th edition, 2018.
- 1066 [78] J. Ohser and K. Schloditz. *3D Images of Materials Structures*. Wiley-VCH, 2009.